

**PHYSICS BASED PROCESS MODELING OF SERRATED CHIP
FORMATION IN PRECISION MACHINING OF DUCTILE ALLOYS**

By

SURIL SHAH

A thesis submitted to the

School of Graduate Studies

Rutgers, The State University of New Jersey

In partial fulfillment of the requirements

For the degree of

Master of Science

Graduate Program in Industrial and Systems Engineering

Written under the direction of

Dr. Tuğrul Özel

And approved by

New Brunswick, New Jersey

May 2019

ABSTRACT OF THE THESIS

PHYSICS BASED PROCESS MODELING OF SERRATED CHIP FORMATION IN PRECISION MACHINING OF DUCTILE ALLOYS

by SURIL SHAH

Thesis Director:

Dr. Tuğrul Özel

Ductility of the material can be defined as a limit until which a material can be plastically deformed without fracture. Ductile metals and alloys have the ability to withstand the deformation in their specific plastic region. Some of the common ductile metals are aluminum, copper, nickel, titanium and silver. Precision cutting of these metals has wide ranging applications in industry, however it presents challenges due to formation of serrated chips and resulting in process irregularities and instabilities. In this research, specially designed orthogonal cutting tests are utilized on copper 10100 and titanium alloy Ti6Al4V at meaningful combination of cutting conditions (feed, speed and depth of cut). Formation of serrated and segmented chips from these experiments are investigated with digital optical microscopy to study morphology and degree of serration. An analytical model is developed to calculate shear stress, shear strain, and shear strain rate from the measured forces and chip dimensions. Finite element (FE) simulations are designed to compare the simulated output data (forces, stress, strain) with the analytical model and the experimental data. Specifically, constitutive material modeling using Johnson-Cook model, flow softening and/or ductile failure are employed where suitable in FE simulations. We developed a methodology to identify a proper set of Johnson-Cook material constitutive model parameters, flow softening behavior, failure and damage models for the purpose of simulating

serrated chip formation process in orthogonal cutting conditions. It is demonstrated that, segmentation of chip, cutting forces, shear stress and shear strain rate can be predicted from the simulations of the machining process rather than conducting actual experiments.

ACKNOWLEDGMENTS

First, I would like to express my deepest gratitude towards my M.S. thesis advisor, Dr. Tuğrul Özel for his endless research work support, insightful guidance and motivation throughout this study. I feel myself lucky to have an opportunity to work with him during my master's coursework.

I appreciate the advice and constructive suggestions I received from my M.S. thesis committee members, Dr. David Coit and Dr. James Luxhøj. I would also like to thank Dr. Melike-Baykal Gursoy and Dr. Myong K. Jeong, who served as ISE graduate directors at Rutgers, for all their support.

I cannot thank enough my colleagues, Mr. Kaushalendra Patel and Mr. Guoliang Liu. Their help and technical support was significant at different parts of this research work.

I appreciate the support I received from the administrators of ISE department at Rutgers, Ms. Cindy Ielmini, Ms. Barthi Ponnuraj, and Ms. Laura Kasica.

Finally, I want to thank my family and close friends for having faith in me and their constant motivation.

DEDICATION

To my parents and “Karina”

For their constant support and love from long distance

TABLE OF CONTENTS

ABSTRACT OF THE THESIS	ii
ACKNOWLEDGMENTS	iv
DEDICATION	v
TABLE OF CONTENTS	vi
LIST OF FIGURES	ix
LIST OF TABLES	x
LIST OF SYMBOLS.....	xi
CHAPTER 1 INTRODUCTION	1
1.1 Basics of Metal Cutting.....	3
1.2 Orthogonal Cutting	4
1.3 Chip Formation Mechanism.....	6
1.4 Shear Zones in Orthogonal Cutting	8
1.5 Field Variables in Orthogonal Cutting	9
CHAPTER 2 ANALYTICAL MODEL FOR SERRATED CHIP FORMATION	12
2.1 Shear Strain and Strain Rate in Primary Deformation Zone	12
2.2 Specific Cutting Forces and Shear Yield Stress	14
CHAPTER 3 EXPERIMENTAL STUDY	15
3.1 Work Material	15
3.2 Orthogonal Cutting Experiments.....	16

3.3 Force and Chip Measurements	17
3.4 Analytical Model Results.....	19
CHAPTER 4 PHYSICS-BASED PROCESS SIMULATION FOR TITANIUM ALLOY Ti6Al4V.....	20
4.1 Finite Element Modeling – An Introduction	20
4.2 Serrated Chip Formation Simulation Model using Abaqus/Explicit	21
4.2.1 Friction Consideration in Simulation Model.....	22
4.3 Work Material Constitutive Models	24
4.3.1 Johnson-Cook Material Constitutive Model	25
4.4 Material Failure and Damage Theory	26
4.5 Damage Initiation and Damage Evolution using Abaqus	28
4.6 Johnson-Cook Failure and Damage Model	29
4.6.1 JC failure model parameters for titanium alloy Ti6Al4V	29
4.7 Results and Discussions.....	30
CHAPTER 5 PHYSICS BASED PROCESS SIMULATION FOR COPPER 10100.....	34
5.1 Finite Element Simulations using Deform-2D	34
5.2 Designing Serrated Chip Formation Simulation using Deform-2D	35
5.3 Constitutive Material Model for Copper 10100.....	36
5.3.1 Identification of JC material model parameters for copper 10100.....	37
5.3.2 Modified material model with temperature dependent parameters and strain softening	39

5.4 Consideration of Friction and Damage	41
5.5 Results and Discussions.....	42
CHAPTER 6 CONCLUSION AND CONTRIBUTIONS.....	46
REFERENCES	48
APPENDIX A	52

LIST OF FIGURES

Figure 1.1 Turning of a metal alloy using lathe tooling (a) (Source: Wikipedia), precision turning of copper (b) (Source: University of Cambridge, Centre for Doctoral Training in Ultra Precision Engineering).	2
Figure 1.2 The basic cutting geometry a) orthogonal cutting, b) oblique cutting (Boothroyd, 1981).	4
Figure 1.3 Geometry of orthogonal cutting model (continuous chip).....	5
Figure 1.4 Types of chip formation in orthogonal cutting; a) continuous, b) discontinuous, c) continuous with built-up edge, d) serrated chips (continuous). (Childs et al., 2000)	6
Figure 1.5 Deformation zones in orthogonal cutting.	8
Figure 1.6 Force diagram in orthogonal cutting.	9
Figure 1.7 Velocity diagram in orthogonal cutting.	10
Figure 2.1 Serrated chip formation model (Özel & Ulutan 2014).	13
Figure 3.1 Chip measurements from microscope image; minimum and maximum chip thickness (t_{min} and t_{max}), pitch (p), and shear angle (ϕ).	18
Figure 4.1 An example for metal cutting simulation using the Lagrangian approach with Abaqus/Explicit (Özel et al., 2007).....	21
Figure 4.2 Finite element simulation model of orthogonal cutting defined in Abaqus/Explicit.	22
Figure 4.3 Material ductile failure process.	27
Figure 4.4 Comparison of experimental and simulated forces for titanium alloy Ti6Al4V cutting conditions.	31
Figure 4.5 Comparative studies of experimental and simulated chips.	33
Figure 5.1 Workpiece and tool mesh using Deform-2D.	35
Figure 5.2 Graphical representation defining the methodology to obtain JC parameters.	38
Figure 5.3 Flow stress curve for given JC parameters at room temperature (20 °C).	39
Figure 5.4 Thermal softening flow stress curves at temperature.	40
Figure 5.5 Comparison of experimental and simulated forces for copper 10100.....	43
Figure 5.6 Comparative study of experimental and simulated chips for copper 10100...	45

LIST OF TABLES

Table 3.1 Chemical composition of titanium alloy Ti6Al4V.....	15
Table 3.2 Chemical composition of copper 10100.	15
Table 3.3 Cutting conditions for copper 10100	16
Table 3.4 Cutting conditions for titanium alloy Ti6Al4V.....	17
Table 3.5 Force and chip measured for copper 10100.	18
Table 3.6 Force and chip dimensions measured for titanium alloy Ti6Al4V.	18
Table 3.7 Calculated shear strain and shear yield stress for copper 10100.	19
Table 3.8 Shear strain and shear yield stress for titanium alloy Ti6Al4V.	19
Table 4.1 Thermal and mechanical properties (at room temperature 20°).....	24
Table 4.2 The Johnson-Cook material model parameters for titanium alloy Ti6Al4V.	26
Table 4.3 The JC material failure model parameters for titanium alloy Ti6Al4V.....	30
Table 4.4 The results of measured and simulated thicknesses and pitch values of serrated chips.	32
Table 5.1 Thermal and mechanical properties (at room temperature 20°).	36
Table 5.2 The Johnson-Cook material model parameters for copper 10100.....	38
Table 5.3 Thermal softening parameters determined for copper 10100.	41
Table 5.4 The results of measured and simulated thickness values for serrated chips of copper 10100.	44

LIST OF SYMBOLS

γ_1	Rake angle [°]
$\dot{\gamma}$	Shear strain rate [1/sec]
δ_{sb}	Shear band thickness [mm]
ϕ_{seg}	Segmented shear angle [°]
μ	Friction coefficient [-]
b	width of cut [mm]
f	Feed rate [mm/rev]
F_c	Cutting force [N]
F_p	Force parallel to shear plane [N]
F_s	Force normal to shear plane [N]
F_t	Thrust force [N]
p	Pitch distance in serrated chips [mm]
R	Fracture toughness [N/mm ²]
S	Spindle speed [rev/min]
t	Undeformed chip thickness [mm]
t_{avg}	Average chip thickness [mm]
t_c	Chip thickness [mm]
t_{max}	Maximum chip thickness [mm]
t_{min}	Minimum chip thickness [mm]
v_c	Cutting velocity [m/min]
v_{ch}	Chip velocity [m/min]
v_s	Shear velocity [m/min]
α	Clearance angle [°]
γ	Shear strain [-]
σ	Normal stress [N/mm ²]
τ	Shear stress [N/mm ²]
τ_y	Shear yield stress [N/mm ²]
ϕ	Shear angle [°]

CHAPTER 1

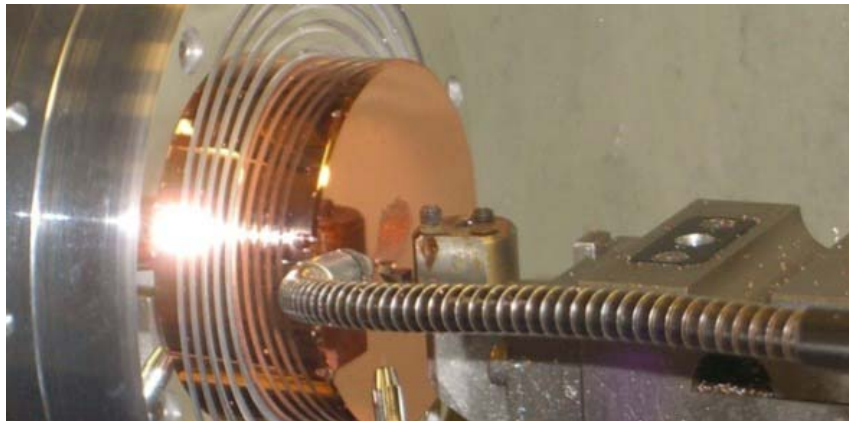
INTRODUCTION

Metal cutting is the process where unwanted material of the metal is removed in form of chips with the use of proper cutting tools to get workpiece in required dimensions and surface finish. Metal cutting results in two products, unwanted material (namely chips) and finished material (final product). As per cutting tool market report (CTMR), in USA, there is solid increase of 12.9% in consumption of cutting tool in 2018 than the previous year (Source: U.S. Cutting Tool Institute and The Association for Manufacturing Technology). The increasing demand of machine tools reflects flexibility and highly precise nature of metal cutting processes. Turning, drilling and milling are the three main type of metal cutting processes heavily used in many industries every year.

Turning is a versatile process where cutting of cylindrical shaped workpiece is done with the use of single point wedge shaped cutting tool. In this process, workpiece is rotated on the spindle and cutting tool moves forward radially, axially or in both directions. A sample of turning process is shown in Figure 1.1.



(a)



(b)

Figure 1.1 Turning of a metal alloy using lathe tooling (a) (Source: Wikipedia), precision turning of copper (b) (Source: University of Cambridge, Centre for Doctoral Training in Ultra Precision Engineering).

A lathe or computer numerically control (CNC) turning center is a type of machine which rotates workpiece held in a chuck rigidly, so that when cutting tools are exerted on the workpiece, it can be manufactured in a shape which has rotational symmetry about axis of rotation. These types of machines consist of mainly four parts: bed, tool carriage, headstock and tailstock. The headstock of the machine holds the workpiece with required amount of pressure with the help of suitable

number and type of jaws. The high-speed rotation of the workpiece with the spindle provide energy to cut the material. Tool carriage consists of different types of required tool for the machining of a workpiece. It can be moved precisely, parallel or perpendicular to the axis of rotation as per required cutting. The bed gives rigid support to the machine, making sure that movement of workpiece and tool is precise. Tailstock of the machine is centered same as the rotational axis of spindle, which provides external support to the long cylindrical bars. In modern CNC machines, other machining operations can also be executed by using proper jigs and fixtures.

1.1 Basics of Metal Cutting

There are two basic configurations of cutting can be defined; (i) orthogonal cutting and (ii) oblique cutting as illustrated in Figure 1.2. These simplified configurations enable analytical modeling of the cutting processes. In orthogonal cutting, often refers to two dimensional (2D) cutting, cutting edge is perpendicular (at 90°) to the direction of motion (or cutting velocity direction). The chips are generated in a direction normal to the cutting edge of the insert (cutting edge). While in oblique cutting (3D cutting), cutting edge is inclined at an angle which is called an acute angle to the direction of feed. The chip flows in a direction at an angle with normal to the cutting edge. In orthogonal cutting, heat developed per unit area is more in contrast with oblique cutting, which results in smaller life of tool in orthogonal cutting. Orthogonal cutting represents only a small part of machining process. However, it is widely used in theoretical and experimental work due to its simplicity and 2D nature as many of the independent variables can be eliminated during calculation.

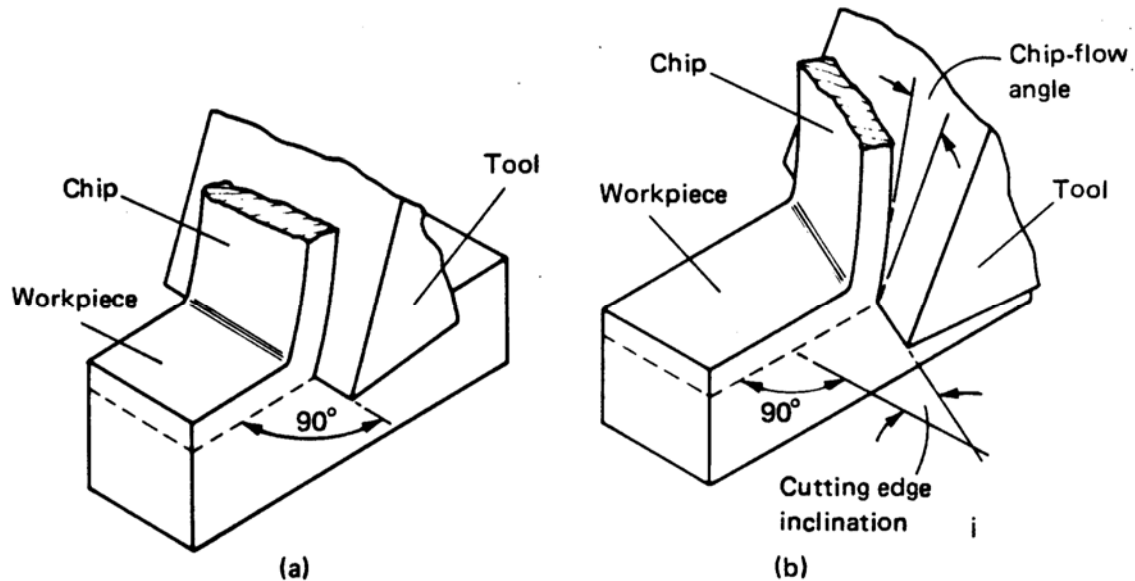


Figure 1.2 The basic cutting geometry a) orthogonal cutting, b) oblique cutting (Boothroyd, 1981).

1.2 Orthogonal Cutting

Orthogonal metal cutting is the most basic metal cutting processes which allows the basic chip formation mechanism to be studied. The following process parameters define the orthogonal cutting process.

- i) *Cutting speed*, v_c , is the relative speed between workpiece and tool in the direction of cutting.
- ii) *Undeformed chip thickness*, t , is the thickness of the workpiece that needs to be removed. It is measured in orthogonal direction to the feed.

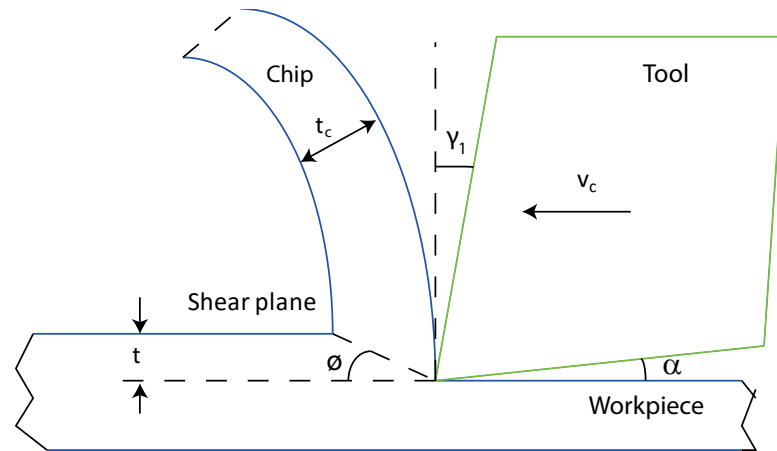


Figure 1.3 Geometry of orthogonal cutting model (continuous chip).

- iii) *Clearance angle*, α , is defined as the angle between clearance face of the tool and work surface.
- iv) *Shear plane* is defined as the plane along which shearing takes place when tool is forced into work material and chip is formed.
- v) *Shear angle*, ϕ is defined as the angle between shear plane and cutting speed vector.

Workpiece materials used in metal cutting falls into two major categories; i) ferrous metals, and ii) nonferrous metals. Nonferrous metals such as copper alloys, aluminum alloy, and titanium alloys and have a wide range of applications. For example, titanium and its alloys are extensively used lightweight applications due to their high strength to weight ratio. Copper and its alloys are used in electrical, automotive, and telecommunication industries. Despite having high malleability and good resistant to corrosion, some of the nonferrous materials are considered difficult-to-cut. Titanium and its alloys are difficult-to-cut due to formation of serrated chips or chips with built up edge and their work hardening nature. Though it is easy to cut copper alloys such as brass with added lead, the toxic nature of lead has raised environmental concerns. This research is concerned with investigating the cutting process for ductile metal alloys i.e. copper alloy 10100 and titanium alloy Ti6Al4V with suitable cutting tools to obtain predictive physics

based cutting models. An adequate simulation model for orthogonal cutting could provide benefits in revealing mechanisms of the cutting process as end-users may easily assess machining quality without having to conduct expensive and time-consuming physical or computational experiments.

1.3 Chip Formation Mechanism

Modeling of chip formation has been of interest to researchers and scientists for decades. Microscopic images of chips have been used heavily to observe the different types of metal cutting processes. High speed motion photographs are used in addition to microscopic images, to distinguish four types of chips which are continuous, discontinuous and continuous with built up edge (see Figure 1.4).

The type of chip formation depends upon properties of workpiece material, cutting conditions (speed, feed and depth of cut), tool geometry and ambient temperature of process.

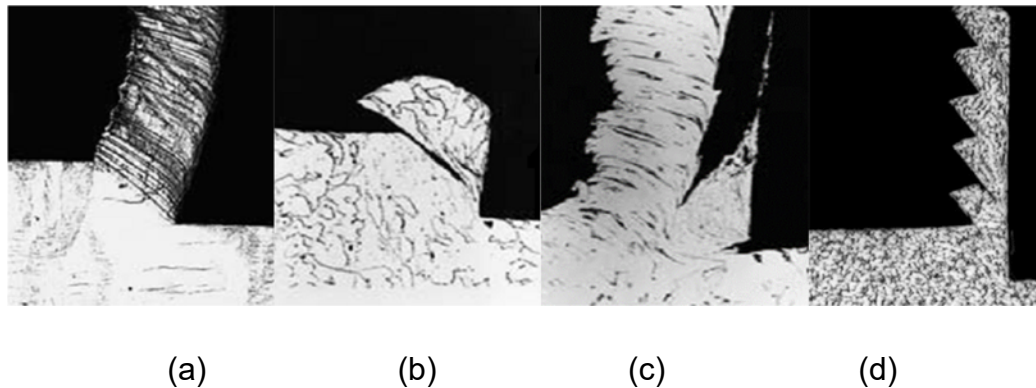


Figure 1.4 Types of chip formation in orthogonal cutting; a) continuous, b) discontinuous, c) continuous with built-up edge, d) serrated chips (continuous) (Childs et al., 2000).

Continuous chip formation is produced during cutting of ductile materials such as brass, copper, low carbon steel and aluminum alloys at high cutting speeds. The tool moves forward to the material which is deformed plastically. In continuous chip

formation model, the workpiece material is accounted to both compression and shear.

Discontinuous chip formation is occurred ahead of the tool and the chip has the appearance of being made of many segments (Figure 1.4(b)) the resulting machined surface is rough and irregular. There is a crack formation in the deforming zone ahead of cutting edge. The crack travels with further advancement of tool and results in formation of small lumps of chip. These lumps start moving up with the chip. The friction force blocks the motion of crack and lumps. The fragment of chip gets detached. The heat generated in cutting area is mostly carried by the chip and thus it results in increasing tool life due to maintained temperature in cutting zone. This type of chip usually occurs when machining brittle materials, however, under certain conditions, for example slow cutting speeds and high negative rake angles, it can occur while machining ductile materials also.

Continuous chip formation with built up edge, tends to occur at intermediate cutting speeds when machining ductile materials but it is difficult to specify any rules for its occurrence. This is the built-up edge which can sometimes be observed welded to the cutting edge after a machining operation. It was shown that built-up edge formation is cyclic in nature with the edge building up to a certain size before becoming unstable and then breaking off.

Serrated chip formation, also known as segmented chip formation, is formation of semi-continuous chip segments, with zones of low and high shear strain. These chips have sawtooth like appearance. They generally occur in metals with low thermal conductivity and strength that decreases sharply with temperature, such as titanium alloys. In some materials, crack initiation due to severe shearing is also observed.

Here, only continuous chips generated while machining can be taken as steady state process. Therefore, it is the process which is assumed to apply in most machining analysis. When the built-up edge formation or serrated chip is occurred, they are difficult to analyze due to their non-steady state nature.

1.4 Shear Zones in Orthogonal Cutting

There are mainly two types of deformation zones formed, primary shear zone and secondary shear zone in orthogonal cutting as shown in Figure 1.5. Though size, shear angle value and other parameters in figure are not accurate, we can have a basic idea about the location of two deformation zones.

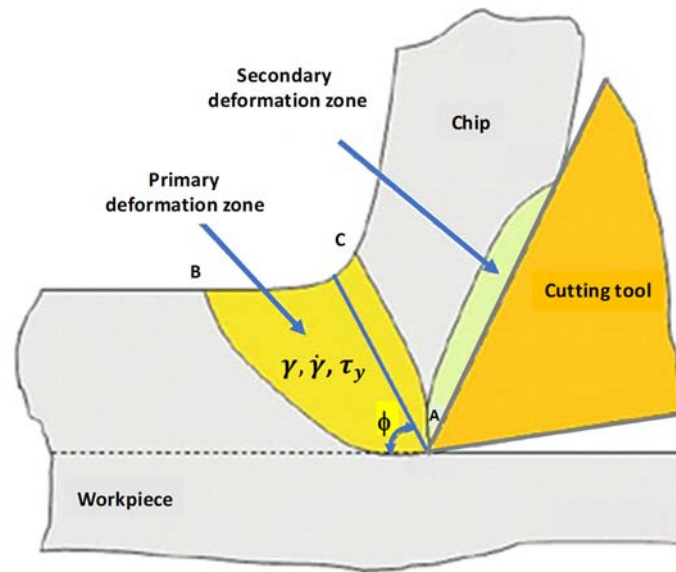


Figure 1.5 Deformation zones in orthogonal cutting.

The primary deformation zone is where the workpiece undergoes major deformations and shearing, and as a result a chip begins to form. The secondary shear zone along the tool rake face is divided into two regions; i) sticking region and ii) sliding region. In the sticking region, chip material tends to adhere to the tool rake face and additional shearing of the chip is observed. In the sliding zone, the chip material slides along the tool rake face. Both shear zones are observed by temperature rise due to severe plastic deformation in primary shear zone and due to friction in secondary zone. Strain hardening due to deformation and softening due to temperature alter the chip formation characteristics in every step of its formation.

1.5 Field Variables in Orthogonal Cutting

In the deformation zones, there are field variables can be defined such as strain, strain rate, stress, and temperature. These are the results of forces in orthogonal cutting process.

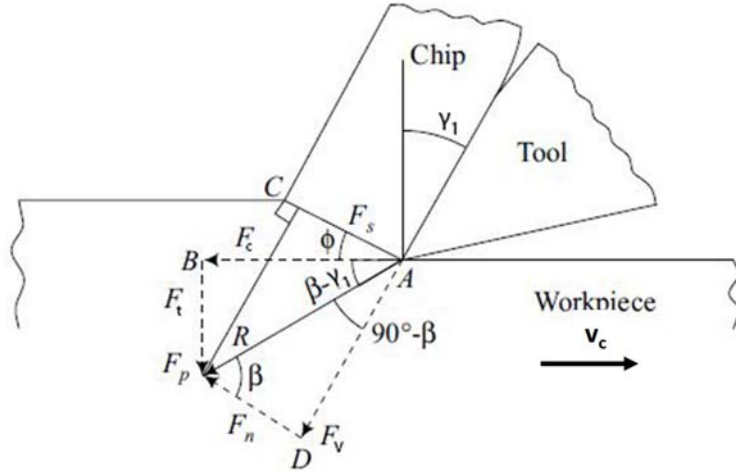


Figure 1.6 Force diagram in orthogonal cutting.

The forces can be represented in two components of the resultant cutting force as, cutting force and thrust force respectively (Fig. 1.6),

$$F_c = \frac{t b \tau_y \cos(\beta - \gamma_1)}{\sin\phi \cos(\phi + \beta - \gamma_1)} \quad (1.1)$$

$$F_t = \frac{t b \tau_y \sin(\beta - \gamma_1)}{\sin\phi \cos(\phi + \beta - \gamma_1)} \quad (1.2)$$

Where, τ_y is the shear stress in the shear plane assumed uniform over this plane and equal to shear yield stress of the workpiece material. In these equations, ϕ is the shear angle, γ_1 is tool rake angle, t is the undeformed chip thickness, b is the width of cut and β is the friction angle.

From the force diagram, forces normal and parallel to shear plan are given by,

$$F_p = F_c \sin\phi + F_t \cos\phi \quad (1.3)$$

$$F_s = F_c \cos\phi - F_t \sin\phi \quad (1.4)$$

While shear stress and normal stress can be obtained with the help of following equations.

$$\tau = \frac{F_s}{A_s} = \frac{(F_c \cos \phi - F_t \sin \phi) \sin \phi}{b t} \quad (1.5)$$

$$\sigma = \frac{(F_c \sin \phi + F_t \cos \phi) \sin \phi}{b t} \quad (1.6)$$

Shear strain and shear strain rate are given respectively by the following equations,

$$\gamma = \tan (\phi - \gamma_1) + \cot \phi \quad (1.7)$$

$$\dot{\gamma} = \frac{V_s}{\Delta y} = \frac{\cos \gamma_1}{\cos (\phi - \gamma_1)} \frac{V_c}{\Delta y} \quad (1.8)$$

where, Δy is the thickness of shear zone.

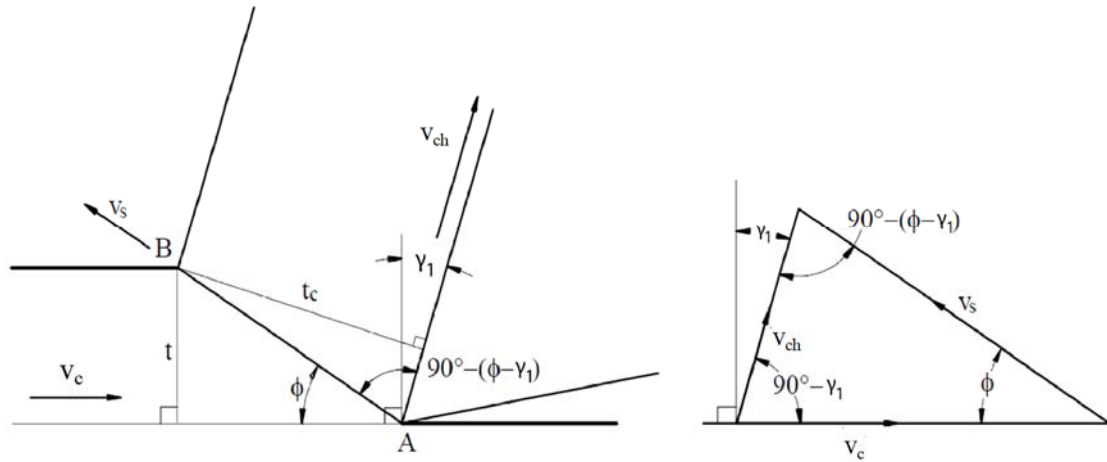


Figure 1.7 Velocity diagram in orthogonal cutting.

From the velocity diagram in Fig. 1.7, chip velocity and shear velocity can be obtained by using the following equations,

$$v_{ch} = \frac{\sin \phi}{\cos (\phi - \gamma_1)} v_c = r v_c \quad (1.9)$$

$$v_s = \frac{\cos \gamma_1}{\cos (\phi - \gamma_1)} v_c \quad (1.10)$$

The contact between the tool and the chip is defined with a friction coefficient and the following formula can be obtained from the force diagram shown in Fig. 1.6.

$$\mu = \frac{F_v}{F_n} = \frac{F_c \sin \gamma_1 + F_t \cos \gamma_1}{F_c \cos \gamma_1 - F_t \sin \gamma_1} = \tan \beta \quad (1.11)$$

Where F_v is the friction force on the rake face, F_n is the normal force on the rake face.

CHAPTER 2

ANALYTICAL MODEL FOR SERRATED CHIP FORMATION

This chapter focuses on description of analytical modeling for serrated chip formation. The orthogonal cutting model given previously is limited to the continuous chip formation (without chip serration) scenario in machining. Many researchers investigated the mechanics and dynamics of serrated chip formation when cutting ductile alloys such as copper and titanium alloys. Cotterell & Byrne (2008) have investigated the dynamics of chip formation and the relation between cutting parameters and chip formation in titanium alloy Ti6Al4V. Fang et al. (2004) provided a segmented chip formation model and investigated chip formation mechanics in machining of aluminum alloys. In this thesis, we will utilize a segmented chip formation model that is similar to model used by Özel & Ulutan (2014). This model is combination of the model presented by Cotterell & Byrne (2008), Pawade et al. (2007), Fang et al. (2004), and Subbaih & Melkote (2007).

2.1 Shear Strain and Strain Rate in Primary Deformation Zone

In this model, the serration of the chip creates a saw-tooth shape. Some parameters such as the pitch of these chips and the shear band thickness plays crucial role in determining the shear strain at the adiabatic shear band. Also, the chip morphology will have peaks and valleys, which makes measurement of chip thickness more difficult. Instead, the minimum chip thickness and maximum chip thickness of a sample is measured, and the arithmetic average of these two is accepted to be the experimental chip thickness.

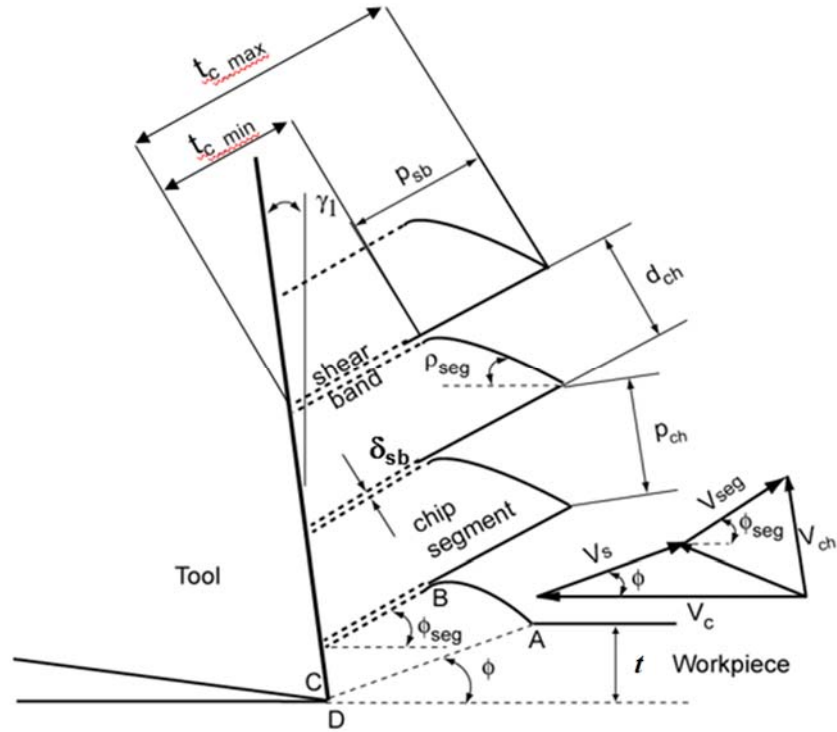


Figure 2.1 Serrated chip formation model (Özel & Ulutan 2014).

The chip ratio (r_c) is defined by the ratio of undeformed chip thickness (t) (or feed in orthogonal cutting) to the average thickness of the segmented chips (t_{avg}) that are measured experimentally,

$$r_c = \frac{t}{t_{avg}} \quad (2.1)$$

Hence, the shear angle can be obtained from measured chip ratios using following equation,

$$\phi = \text{atan} \left(\frac{r_c \cos(\gamma_1)}{1 - r_c \sin(\gamma_1)} \right) \quad (2.2)$$

Following this equation, the shear strain in primary zone (Fig. 1.5) can be found and the calculation based on continuous chip formation model becomes

$$\gamma = \frac{\cos(\gamma_1)}{\sin(\phi) \cos(\phi - \gamma_1)} \quad (2.3)$$

In addition, average strain rate based on segmented chip calculations becomes as,

$$\dot{\gamma} = \frac{\cos(\gamma_1)}{\sin(\phi - \gamma_1)} \frac{v_c}{\delta_{sb}} \quad (2.4)$$

2.2 Specific Cutting Forces and Shear Yield Stress

The cutting forces in machining of ductile alloys depend on the cutting conditions such as cutting speed and feeds. The highest forces are encountered at lower cutting speeds and feeds. The essential result for this observation is the increasing specific energy for shearing and the material separation as suggested by Subbaih & Melkote (2007) as an extension to Atkins model (Atkins 2005), which will be utilized to find the shear yield stress.

In this model, the cutting force is assumed to be equal to a linear trend with an intercept and slope as given in the following equation,

$$F_c = \left(\frac{\tau_y \gamma b}{Q} \right) t + \frac{R b}{Q} \quad (2.5)$$

Here, the parameter Q is the common denominator presented by,

$$Q = 1 - \frac{\sin(\beta)\sin(\phi)}{\cos(\beta - \gamma_1)\cos(\phi - \gamma_1)} \quad (2.6)$$

Where,

$$\beta = \gamma_1 + \tan^{-1} \left(\frac{F_t}{F_c} \right) \quad (2.7)$$

Then, various meaningful combinations of R and τ_y are created, and all of the combinations are subjected to calculation of $I = \frac{R b}{Q}$ and $S = \frac{\tau_y \gamma b}{Q}$ which are the intercepts and slopes of the force graphs. When the ratio of (I/S) calculated this way is equal to the ratio calculated from the force measurements, the calculation is ended and fracture toughness (R) and shear yield stress (τ_y) of the material are obtained, as well as the shear angle (ϕ). The calculated shear yield stress and shear strain can be obtained which will be used as input to the Finite Element simulations.

CHAPTER 3

EXPERIMENTAL STUDY

3.1 Work Material

In a research related to manufacturing processes, experimental results are of great value. It is difficult and time consuming to set up and conducting experiments. For these reasons, it is important to utilize some experimental results already gathered by other researchers in modeling studies rather than designing and conducting all experiments within the same study. In this thesis, experimental results from qualified researchers were utilized in addition to the experiments conducted within the scope of this project.

This experimental work includes orthogonal cutting tests, where the tool and workpiece interaction results in chip formation that can be assumed in two-dimensional plane. The deformations in the third dimension are often negligible in this configuration, such that measured forces in the third dimension are usually not even reported. This type of machining is not frequently used in industry, but force and temperature measurements are gathered from these experiments that can be utilized in developing physics-based analytical process models.

Before describing details of experimental procedures and results, chemical composition of metal alloys has been studied, and their compositions are given in Tables 3.1 and 3.2.

Table 3.1 Chemical composition of titanium alloy Ti6Al4V.

Element	Ti	Al	V	Fe	O	C	N	H	Others
%	Balance	6	4	0.25	0.13	0.08	0.03	0.01	0.4

Table 3.2 Chemical composition of copper 10100.

Element	Pure Copper	Oxygen Content
%	99.99	0.0005

3.2 Orthogonal Cutting Experiments

Orthogonal cutting experiments are very easy to understand in most cases, where machining occurs by removal of material due to coupled motion of the tool and workpiece in orthogonal directions. The third dimension does not affect the machining process significantly as forces in experiments are divided by the width of cut in these experiments, which is the thickness of machined workpiece in third dimension. A three-dimensional illustration of the process is not necessary, since the process is symmetric in the third dimension. Depth of cut is equivalent to feed rate, the tool motion in that direction. Cutting speed (v_c) is a result of workpiece rotation, but since this is a relative motion, one can also consider the workpiece as constant and the tool moving towards the workpiece with cutting speed. The force component in this direction is called the cutting force (F_c), while the force component in the direction of width of cut is called thrust force (F_t).

The experiments obtained for cutting copper 10100 were performed with cutting tools from synthetic diamond material with an edge radius of $0.1\ \mu\text{m}$. In the cutting tests, a neutral rake angle ($\gamma_1 = 0^\circ$) tool holder was used and cutting speeds of $v_c = 1.98\ \text{m/min}$, $v_c = 3.96\ \text{m/min}$ and $v_c = 10.02\ \text{m/min}$ at uncut chip thickness values of $t = 30\ \mu\text{m}$ and $t = 50\ \mu\text{m}$ were applied as given in Table 3.3.

Table 3.3 Cutting conditions for copper 10100.

No.	Tool Material	Rake angle, γ_1 [degree]	Cutting speed, v_c [m/min]	Feed t [mm/rev]
1	Diamond	0	1.98	0.03
2	Diamond	0	1.98	0.05
3	Diamond	0	3.96	0.03
4	Diamond	0	3.96	0.05
5	Diamond	0	10.02	0.03
6	Diamond	0	10.02	0.05

In this study, previously conducted orthogonal cutting tests are utilized. Orthogonal cutting experiments for titanium alloy Ti6Al4V were performed using carbide tools (WC/Co) as uncoated with an edge radius around $r_\beta = 5\ \mu\text{m}$ and coated with TiAlN material with an edge radius around $r_\beta = 10\ \mu\text{m}$ (Sima and Özel 2010). In the cutting

tests, a neutral rake angle ($\gamma_1 = 0^\circ$) tool holders was used and cutting speeds of $v_c = 121.9$ m/min and $v_c = 240.8$ m/min at uncut chip thickness (feed) values of $t = 0.1016$ mm/rev and $t = 0.127$ mm/rev were employed under dry cutting conditions (no lubricant or coolant applied). The specific experimental design is shown in Table 3.4.

Table 3.4 Cutting conditions for titanium alloy Ti6Al4V.

No.	Tool Material	Rake angle, γ_1 [°]	Cutting speed, v_c [m/min]	Feed, t [mm/rev]
1	Uncoated WC/Co	0	121.9	0.102
2	Uncoated WC/Co	0	121.9	0.127
3	Uncoated WC/Co	0	240.8	0.102
4	Uncoated WC/Co	0	240.8	0.127
5	TiAlN coated WC/Co	0	121.9	0.102
6	TiAlN coated WC/Co	0	121.9	0.127

3.3 Force and Chip Measurements

The cutting forces were measured as replicated twice by using Kistler type dynamometer equipped with charge amplifiers and a proper data acquisition system. These measured forces for both materials are listed in Tables 3.5 and 3.6 and they will be used to develop an analytical model which can compute shear strain and shear yield stress along with chip dimension measurements.

The chips are collected during the test, placed in an epoxy compound, polished and chemically etched for a cross-sectional view to inspect the chip dimensions and chip morphology. Chip dimensional measurements typically involve using metallurgical grade digital optical microscopy images as shown in Fig. 3.1.

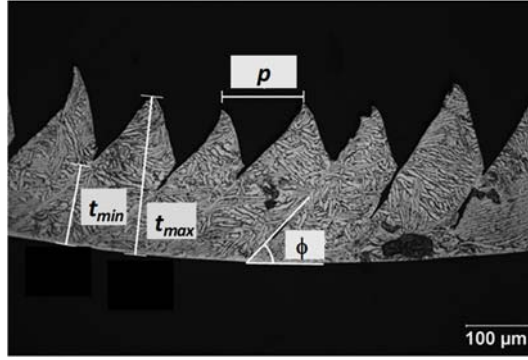


Figure 3.1 Chip measurements from microscope image; minimum and maximum chip thickness (t_{min} and t_{max}), pitch (p), and shear angle (ϕ).

Force and chips data measured for orthogonal cutting of copper 10100 are given in Table 3.5.

Table 3.5 Force and chip measured for copper 10100.

Cutting speed, v_c [m/min]	Feed, t [mm/rev]	Cutting Force, F_c [N]	Thrust Force, F_t [N]	Minimum chip thickness t_{min} [mm]	Maximum chip thickness, t_{max} [mm]
1.98	0.03	116.5	5.3	0.0130	0.0150
1.98	0.05	255.5	34.9	0.0175	0.0275
3.96	0.03	140.9	19.6	0.0260	0.0330
3.96	0.05	230.5	28.0	0.0440	0.0570
10.02	0.03	125.9	11.3	0.0280	0.0330
10.02	0.05	240.0	34.0	0.0360	0.0580

Force and chips data measured for orthogonal cutting of titanium alloy Ti6Al4V are given in Table 3.6.

Table 3.6 Force and chip dimensions measured for titanium alloy Ti6Al4V.

Cutting speed, v_c [m/min]	Feed, t [mm/rev]	Cutting Force, F_c [N/mm]	Thrust Force, F_t [N/mm]	Minimum chip thickness, t_{min} [mm]	Maximum chip thickness, t_{max} [mm]
121.9	0.102	189.15	79.6	0.130	0.192
121.9	0.127	225.01	92.72	0.104	0.177
240.8	0.102	193.48	122.47	0.087	0.160
240.8	0.127	227.16	166.83	0.102	0.186
121.9	0.102	202.29	107.06	0.137	0.182
121.9	0.127	234.2	109.18	0.140	0.216

3.4 Analytical Model Results

Through the experiments, force and chip measurements were obtained which are used to develop an analytical model as described in previous sections. Below are the results for copper 10100 (Table 3.7) and titanium alloy Ti6Al4V (Table 3.8).

Table 3.7 Calculated shear strain and shear yield stress for copper 10100.

Cutting speed, v_c [m/min]	Feed, t [mm/rev]	Shear strain, γ [mm/mm]	Shear stress, τ_y [MPa]	Strain rate, $\dot{\gamma}$ [1/s]
1.98	0.03	1.158	5149.69	27907.5
1.98	0.05	1.195	4628.92	26332.3
3.96	0.03	1.186	4448.99	51402.9
3.96	0.05	1.158	4522.47	33971.8
10.02	0.03	1.165	3126.44	271569.5
10.02	0.05	1.155	2986.96	214532.4

Table 3.8 Shear strain and shear yield stress for titanium alloy Ti6Al4V.

Cutting speed, v_c [m/min]	Feed, t [mm/rev]	Shear strain, γ [mm/mm]	Shear stress, τ_y [MPa]	Strain rate, $\dot{\gamma}$ [1/s]
121.9	0.102	1.578431	689.41	3996056.2
121.9	0.127	1.106299	997.22	3189232.0
240.8	0.102	1.210784	766.07	6634037.9
240.8	0.127	1.133858	803.01	6386822.4
121.9	0.102	1.563725	763.16	3969525.7
121.9	0.127	1.401575	868.68	3682120.8

CHAPTER 4

PHYSICS-BASED PROCESS SIMULATION FOR TITANIUM ALLOY Ti6Al4V

4.1 Finite Element Modeling – An Introduction

Early work of using Finite Element (FE) modeling in cutting processes was carried out beginning with Klamecki (1973) and Tay et al. (1974). Since then FE modeling of machining process has evolved into useful simulation tools. Recent literature review on the FE modeling work can be found in Arrazola et al. (2013) and Melkote et al. (2017).

The FE based simulation models use numerical solution methods including Eulerian and Lagrangian approach. The Lagrangian numerical method is widely used for simulating the chip formation from incipient state to the steady-state with a pre-defined chip geometry assumption. In this type of analysis, mesh grid deforms with the material, while in Eulerian approach the mesh grid is fixed, and the work material flows through it. However, a pre-defined chip geometry is assumed in Eulerian approach. The Lagrangian approach simulates incipient, steady-state, intermittent, and discontinuous chip formation phases while with Eulerian approach this is not possible. In this study, we have used the Lagrangian approach to model orthogonal cutting process with FE simulations and by using Abaqus/Explicit software package (Fig. 4.1).

The Finite Element Analysis (FEA) software is very important to determine the accuracy of simulation results. Among these FEA software, Ansys/LS-Dyna, Abaqus Standard/Explicit, Deform 2D/3D, MSC Marc, and Thirdwave AdvantEdge have been widely used in academia as well as in industry for machining processes. In this study, Abaqus/Explicit and Deform 2D has been used due to its wide acceptance over machining simulations and its nature of providing detailed output for field variables.

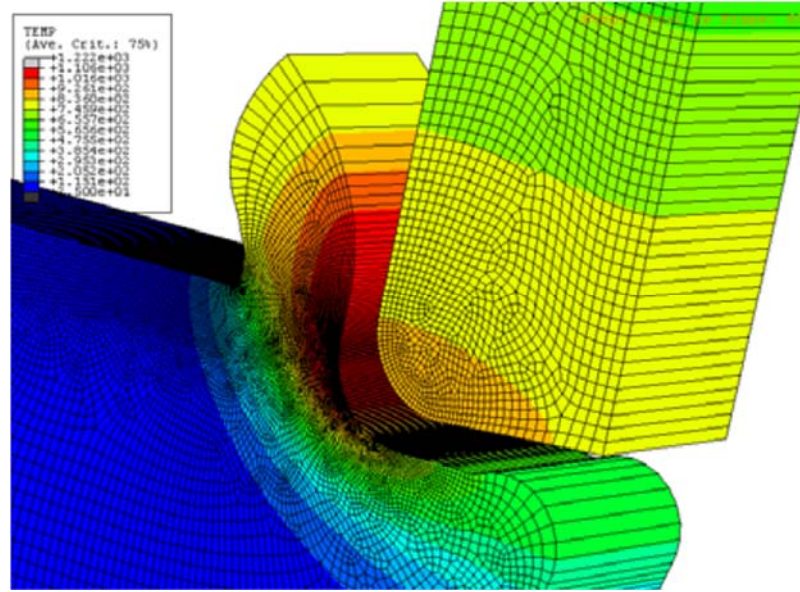


Figure 4.1 An example for metal cutting simulation using the Lagrangian approach with Abaqus/Explicit (Özel et al., 2007).

4.2 Serrated Chip Formation Simulation Model using Abaqus/Explicit

In the serrated chip formation simulations conducted in this study, the workpiece is defined as a rectangular shape, where the cutting length (and speed) is symbolized as an accelerated thermo-mechanical process in the horizontal direction, and the feed is symbolized as the cutting thickness in the vertical direction (uncut chip thickness). The elements that are defined closer to the tool tip are smaller, allowing them to exhibit finer calculations, since the thermal and mechanical process is mostly observed in that region. The elements that are defined far from the tool tip are larger, allowing a smaller number of total elements both in the tool and the workpiece, leading to a significantly decreased simulation time.

The workpiece is created, and then divided into three sections as “Chip”, “Joint”, and “Base”. The thickness of the “Chip” layer is equal to the feed (or uncut chip thickness), “Joint” is modeled as the thin layer to be removed during machining process to generate new surface and chip from workpiece. “Base” is modeled as

the bottom section of the workpiece which is the section left after machining as the machined surface. High density meshing, and failure criterion are only applied to the “Chip” and “Joint” sections to improve the simulation accuracy and speed up the simulation meanwhile (Fig. 4.2).

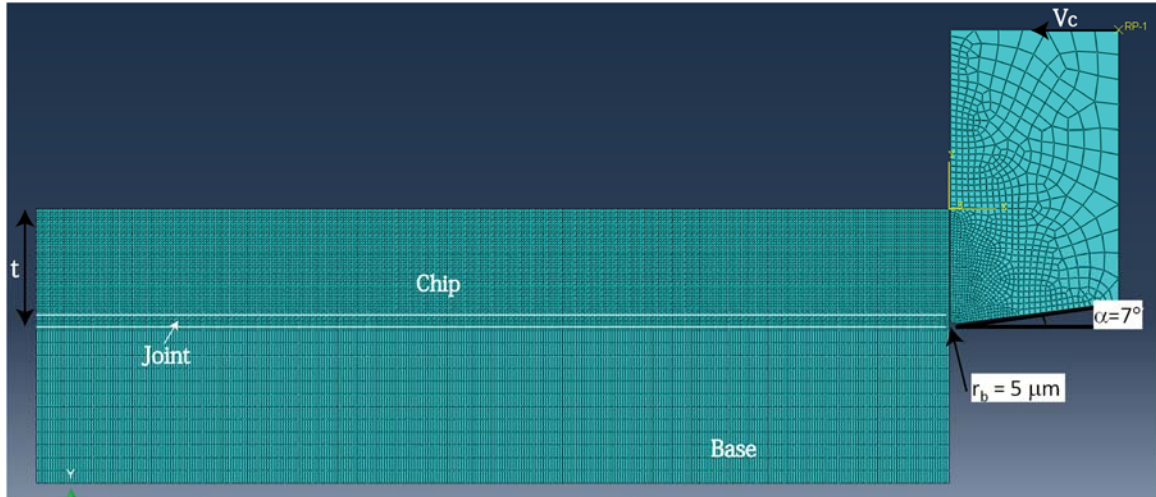


Figure 4.2 Finite element simulation model of orthogonal cutting defined in Abaqus/Explicit.

The coupled temperature-displacement plane strain elements CPE4RT element type is adopted for workpiece, which is characterized with four-node, thermally coupled quadrilateral, bilinear displacement, and temperature, and reduced integration. Work material constitutive models, boundary conditions and simulations controls were implemented as per each cutting condition to the simulation model.

4.2.1 Friction Consideration in Simulation Model

Frictional condition at the tool-chip interfaces is another important factor to be considered for successful Finite Element simulation of metal cutting. As commonly accepted, the shear stress distribution on the tool rake face can be represented as two distinct regions:

1) Along the tool–chip contact area and near the cutting edge, a sticking region forms, and the frictional shearing stress at the sticking region, τ_f , becomes equal to the average shear flow stress at the tool–chip interface on the chip, k_{chip} , $\tau_f = k_{chip}$; (See Eq. 4.1a)

2) Over the remainder of the tool–chip contact area, a sliding region forms, and the frictional shearing stress, τ_f , can be determined by the normal stress distribution over the rake face, σ_n , and coefficient of friction, μ (See Eq. 4.1b) (Pang and Zhao 2017).

(i) In the sticking region:

$$\tau_f(x) = k_{chip}, \text{ when } \mu \cdot \sigma_n(x) \geq k_{chip}, 0 < x \leq l_p \quad (4.1a)$$

(ii) In the sliding region:

$$\tau_f(x) = \mu \cdot \sigma_n(x), \text{ when } \mu \cdot \sigma_n(x) < k_{chip}, l_p < x \leq l_c \quad (4.1b)$$

where l_p is the length of the sticking region and l_c is the chip–tool contact length.

In the FE simulation model, sticking and sliding regions are defined by utilizing the limiting shear stress as k_{chip} and a friction coefficient as μ so that sticking zone ends as soon as shear stress τ_f reaches to the limiting shear stress and sliding contact becomes effective automatically according to the simulation condition.

In the previous work, the friction coefficient of $\mu = 0.5$ was used for both coated and uncoated carbide tools (Sima and Özel 2010). In fact, the TiAlN coating has the function of reducing friction coefficient at higher cutting speeds. Therefore, a friction coefficient of $\mu = 0.6$, proposed by Obikawa et al. (1996), is used in this work for uncoated carbide tool, while a friction coefficient of $\mu = 0.3$, proposed by Calamaz et al. (2008), is adopted for TiAlN coated carbide tool.

In this work, temperature dependent thermal and mechanical properties for workpiece materials (e.g. titanium alloy Ti6Al4V and copper 10100) and tool material (WC/Co tungsten carbide and diamond) are assigned as shown in Table 4.1.

Table 4.1 Thermal and mechanical properties (at room temperature 20°).

Material Properties	Titanium alloy, Ti6Al4V	Carbide tool, WC/Co
Young's modulus [MPa]	113390	56e6
Poisson's ratio	0.31	0.3
Thermal expansion [mm.mm ⁻¹ .°C ⁻¹]	7.06e-006	6.4e-06
Conductivity (W.m ⁻¹ .°C ⁻¹)	7.2	60
Density (kg/mm ³)	4.43e-09	1.3e-08
Specific heat (N.mm kg ⁻¹ °C ⁻¹)	5.263e08	1.85e08

4.3 Work Material Constitutive Models

The advancement in FE modeling and simulation of machining processes has reached to a capability to predict process outputs such as cutting forces, stresses, strains, strain rates, and temperatures generated. However, the accuracy of these predictions relies on the work material constitutive model describing the flow stress, at which work material starts to plastically deform.

Several researchers have proposed specific flow stress material modes in metal cutting. Oxley (1989) proposed that flow stress can be expressed as work hardening behavior as given in Eq. (4.2) where initial yield stress (σ_0) and strain hardening exponent (n) are written as a function of the velocity modified temperature (T_{MOD}) and provided such data for carbon steels. Here, temperature and strain rate are combined into a single function.

$$\bar{\sigma} = \sigma_0 \epsilon^{-n} \quad (4.2)$$

$$T_{MOD} = T [1 - v \log (\frac{\dot{\epsilon}}{\dot{\epsilon}_0})] \quad (4.3)$$

Where σ_0 is initial yield strength, n is the strain hardening index, T is temperature, v is constant, $\dot{\epsilon}$ is strain and $\dot{\epsilon}_0$ is strain rate.

Oxley's model has been utilized in modelling of orthogonal cutting for low and medium carbon steels in conjunction with slip-line field analysis as an analytical approach to predict forces, average strain, strain rate and temperature in primary shear zone (Özel and Zeren 2006; Karpas and Özel 2007).

In recent studies, the Split-Hopkinson pressure bar (SHPB) tests and orthogonal cutting tests in combination with an inverse analysis method have been adopted by researchers to obtain the flow stress data under various strain, strain rates and temperature regimes and further to compute the unknown parameters of the material constitutive models.

Among many other material constitutive models, Johnson-Cook (JC) material model is widely used for high strain rate applications in which models describe the flow stress of a material as functions of strain, strain rate and temperature effects.

4.3.1 Johnson-Cook Material Constitutive Model

The Johnson-Cook model describes the flow stress as the product of strain, strain rate and temperature effects. i.e. work hardening, strain rate hardening, and thermal softening (Johnson & Cook 1983).

$$\bar{\sigma} = [A + B (\bar{\epsilon})^n][1 + C \ln(\frac{\dot{\bar{\epsilon}}}{\dot{\bar{\epsilon}}_0})] [1 - (\frac{T - T_0}{T_m - T_0})^m] \quad (4.4)$$

where, A is initial yield strength of the material at room temperature, $\dot{\bar{\epsilon}}$ is equivalent plastic strain rate, $\dot{\bar{\epsilon}}_0$ is reference strain rate, T_0 is room temperature, T_m is melting temperature, n is strain hardening effect, m is thermal softening effect, C is strain rate sensitivity.

The Johnson-Cook model assumes that the slope of the flow stress curves independently affected by strain hardening, strain rate sensitivity and thermal softening behaviors. Each of these sets is represented by the brackets in the consecutive equation. Several model parameters are available in the literature for titanium alloy Ti6Al4V as given in Table 4.2.

Table 4.2 The Johnson-Cook material model parameters for titanium alloy Ti6Al4V.

JC model parameter	Lee & Lin (1998)	Lee & Lin (1998)	Meyer & Kleponis (2001)	Kay (2002)	Seo et al. (2005)
A	782.7	724.7	862.5	1098	997.9
B	498.4	683.1	331.2	1092	653.1
n	0.028	0.035	0.012	0.014	0.0198
C	0.28	0.47	0.34	0.93	0.45
m	1	1	0.8	1.1	0.7

While, JC parameters given by Lee & Lin (1998) for titanium alloy Ti6Al4V were utilized for the titanium cutting simulations, an analytical approach was used to obtain JC parameters for copper 10100.

4.4 Material Failure and Damage Theory

As mentioned earlier, the capabilities of simulation software reached to the point that they can predict the deformation behavior of materials with high complexity. These models lack failure models which are required in design of engineering components. The reason is that failure is physically a very complicated process. Failure of ductile and brittle materials, both are different and depends on parameters such as strain, temperature etc.

Often times, there are two approaches that are utilized to simulate chip serration in the finite element cutting simulations. The first approach is modeling by considering and using material failure models (Chen et al., 2011, Wang et al. 2016, Childs et al., 2018). The second approach is modeling by considering for temperature-dependent flow softening based material behavior for adiabatic shearing (Calamaz et al., 2008, Sima & Özel 2010) To adopt the first approach, it is important to employ proper material failure models. In recent studies, material ductile failure criteria have been widely implemented by researchers in metal cutting simulations. In recent studies, ductile failure criteria have been widely implemented by researchers in machining simulations (Chen et al., 2011).

The theory of damage mechanics considers the process of material degradation due to the initiation, growth and coalescence of micro-cracks/voids in a material element under monotonic or cyclic impact, or with thermo-mechanical loading. A valid material failure criterion should be taken in to account in the process of progressive material degradation/damage under either static or dynamic/fatigue loading.

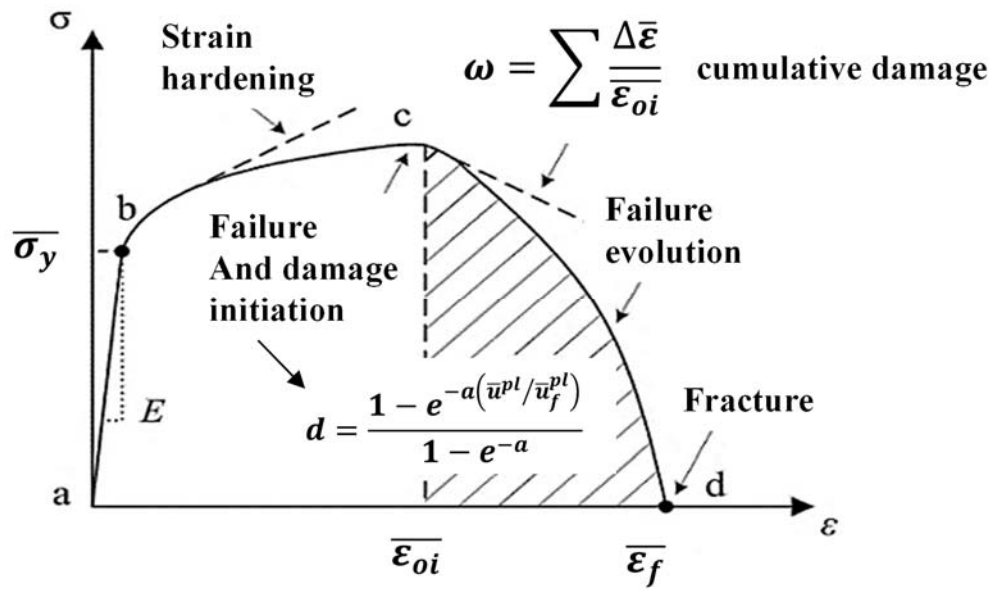


Figure 4.3 Material ductile failure process.

As shown in Fig 4.3, the material ductile failure process has two stages: i) the damage initiation stage and ii) the damage/failure evolution stage as it is related to material separation and chip serration during cutting process. That can be captured and explained through an integrated formulation by using JC constitutive material model, JC material failure model, cumulative damage law and failure/damage evolution.

4.5 Damage Initiation and Damage Evolution using Abaqus

Finite element modeling software, Abaqus/Explicit, offers a general framework for material failure modeling (Zetterberg 2014) that allows the combination of multiple failure mechanisms acting simultaneously on the same material. Material failure refers to the complete loss of load carrying capacity that results from progressive degradation of the material stiffness. The stiffness degradation process is modeled using damage mechanics.

The software also offers a variety of choices of damage initiation criteria for ductile metals, each associated with distinct types of material failure. They can be classified in the following categories:

- Damage initiation criteria for the fracture of metals, including ductile and shear criteria (e.g. ductile damage, or Johnson - Cook damage).
- Damage initiation criteria for the necking instability of sheet metals. These include forming limit diagrams intended to assess the formability of sheet metal material.

In continuum mechanics the constitutive model is normally expressed in terms of stress-strain relations. When the material exhibits strain-softening behavior, leading to strain localization, this formulation results in a strong mesh dependency of the finite element results in that the energy dissipated decreases upon mesh refinement. In Abaqus, all available damage evolution models use a formulation intended to alleviate the mesh dependency. The damage evolution law describes the rate of degradation of the mesh element stiffness once the corresponding initiation criterion has been reached. For damage in ductile metals, Abaqus/Explicit assumes that the degradation of the stiffness associated with each active failure mechanism can be modeled using a scalar damage variable. The value of scalar damage variable (displacement at failure) should be related to minimum element size defined in mesh and can be determined by the trial and error method (Zetterberg 2014).

Among many other material constitutive models, Johnson-Cook (JC) material model is widely used for high strain rate applications in which models describe the flow stress of a material as functions of strain, strain rate and temperature effects.

4.6 Johnson-Cook Failure and Damage Model

According to the classical cumulative damage law, expressed in Eq. (4.5), the material reaches the failure initiation stage at point c when $\omega = 1$.

$$\omega = \sum \frac{\Delta \bar{\epsilon}}{\bar{\epsilon}_{ol}} \quad (4.5)$$

where ω is the state variable, $\Delta \bar{\epsilon}$ is the increment of equivalent plastic strain that occurs during an integration cycle and $\bar{\epsilon}_{ol}$ is the equivalent plastic strain at failure initiation.

Johnson & Cook (1985) proposed the general expression for the equivalent failure strain, i.e. the JC failure model as expressed by Eq. (4.6) by utilizing torsion tests over a range of strain rates, Split-Hopkinson bar tests over a range of temperatures, and quasi-static tensile tests with various notch geometries. The JC failure model has been widely adopted by researchers as the damage initiation criterion in the metal cutting simulations using Abaqus Explicit.

$$\bar{\epsilon}_{ol} = \left[d_1 + d_2 \exp \left(d_3 \frac{p_1}{\bar{\sigma}_v} \right) \right] \left[1 + d_4 \ln \left(\frac{\dot{\bar{\epsilon}}}{\dot{\bar{\epsilon}}_0} \right) \right] \left[1 - d_5 \left(\frac{T - T_r}{T_m - T_r} \right)^m \right] \quad (4.6)$$

In this equation, p_1 is the average of three normal stresses (the hydrostatic pressure), $\bar{\sigma}_v$ is the equivalent von Mises stress, and $\frac{p_1}{\bar{\sigma}}$ is the stress triaxiality. The parameters d_1 , d_2 , d_3 , d_4 , and d_5 are the JC material failure model parameters which are determined by material testing and experiments.

4.6.1 JC failure model parameters for titanium alloy Ti6Al4V

For the simulation of orthogonal cutting titanium alloy Ti6Al4V, it is assumed that both material separation and chip serration are caused by material failure and

damage evolution. The failure and damage evolution models are employed in finite element simulations of 2D orthogonal cutting with plane strain analysis using Abaqus/Explicit software. The values of the JC failure model parameters for titanium alloy Ti6Al4V that are reported as given in Table 4.3. In this study, the failure model parameters obtained by Johnson & Holmquist (1989) have been adopted in the cutting simulations.

Table 4.3 The JC material failure model parameters for titanium alloy Ti6Al4V.

JC failure model parameter	Johnson & Holmquist (1989)	Kay (2002)
d_1	-0.09	-0.09
d_2	0.25	0.014
d_3	-0.5	0.27
d_4	0.014	3.87
d_5	3.87	0.48

4.7 Results and Discussions

All cutting conditions in the orthogonal cutting tests were simulated by using the FE model describe in the previous section. Predicted forces from these FE simulations are compared with measured results as shown in Fig. 4.4, Almost all cutting parameters (cutting speed and feed) and coating condition (uncoated WC/Co or TiAlN coated WC/Co) have important effects on the cutting forces. The cutting forces generally increased with the cutting speed and feed. It was observed that measured thrust forces are increased sustainably at the higher cutting speed at both levels of feed.

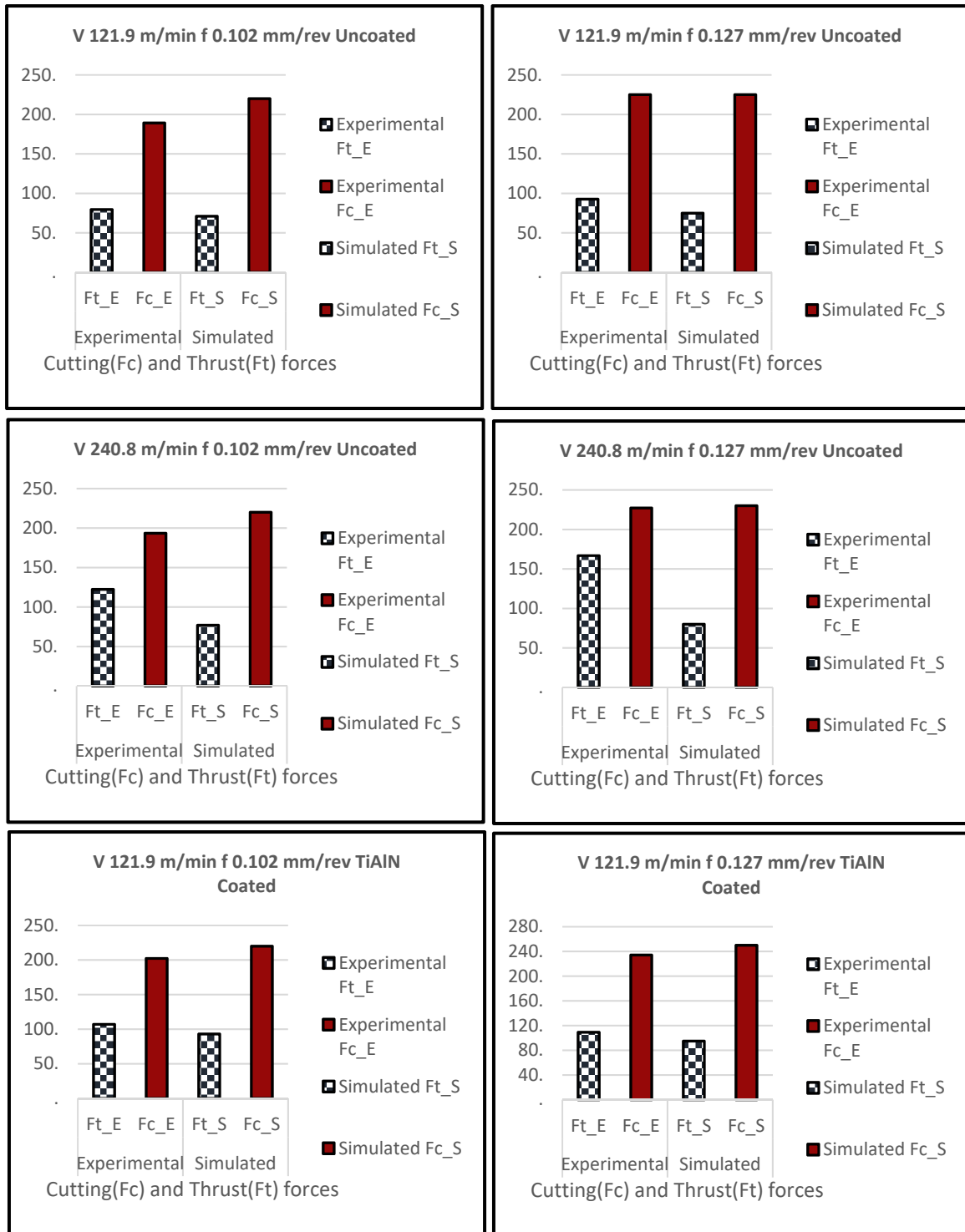


Figure 4.4 Comparison of experimental and simulated forces for titanium alloy Ti6Al4V cutting conditions.

From the comparison of simulated and measured cutting forces in Fig. 4.4, it is obvious that cutting forces are in close agreements within not more than 15% prediction error in most cutting conditions, which proved that this proposed FE simulation model possesses a good accuracy. However, the simulated thrust forces are not all in close agreements with the measured ones. The error between the measured and predicted thrust forces under the cutting speed of 121.9 m/min is mostly not more than 15%, while the error under the cutting speed of 240.8 m/min is rather larger. It has been observed that the higher thrust forces under the high cutting speed are mainly produced by the adhered titanium alloy material at elevated temperatures on the rake face as the heat generation increases, which cannot be easily modeled in the FE simulation and thus this situation results in rather larger prediction error. A detailed comparison of simulated serrated chips with microscopic chip images is shown in Fig. 4.5. The results of measured and simulated serrated chip thicknesses and serration pitch distances are given in Table 4.4. It is observed that almost all simulated chip geometries investigated depict periodic formation of serrated and uniform sized chip segments after a large single segment. In addition, close agreements between the simulated and captured serrated chip shapes and morphologies are observed. It should be noted that the cutting conditions used in these comparisons included the effects of cutting speed, feed and tool coating on the formation of serrated chips.

Table 4.4 The results of measured and simulated thicknesses and pitch values of serrated chips.

Tool material	Rake angle, $\gamma_1(^{\circ})$	Cutting speed, v_c (m/min)	Feed, t_u (mm)	Experimental			Simulation		
				t_{min} (mm)	t_{max} (mm)	P (mm)	t_{min} (mm)	t_{max} (mm)	P (mm)
Uncoated WC/Co	0	240.8	0.102	0.087	0.16	0.08	0.093	0.14	0.055
Uncoated WC/Co	0	240.8	0.127	0.102	0.186	0.095	0.09	0.18	0.086
TiAlN coated WC/Co	0	121.9	0.102	0.137	0.182	0.075	0.09	0.16	0.07
TiAlN coated WC/Co	0	121.9	0.127	0.14	0.216	0.1	0.095	0.19	0.075

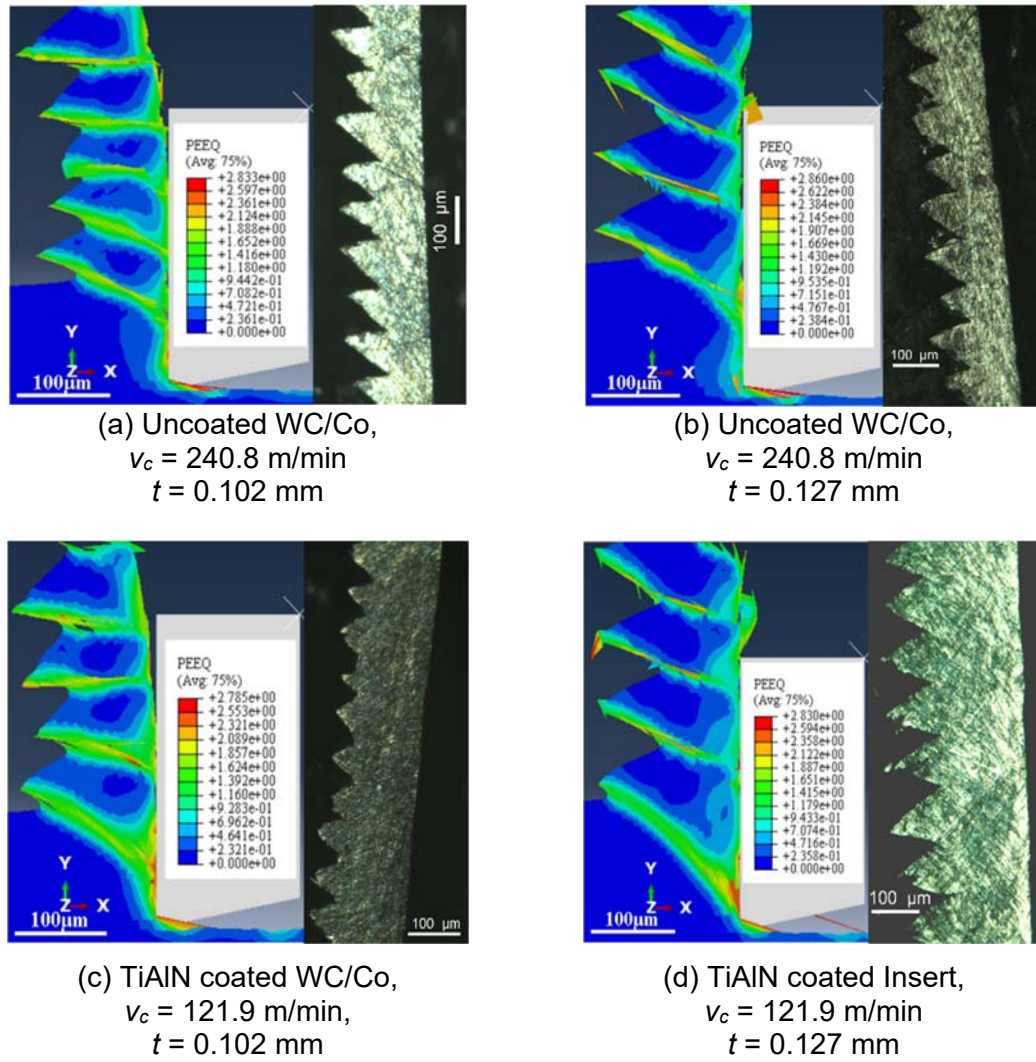


Figure 4.5 Comparative studies of experimental and simulated chips.

CHAPTER 5

PHYSICS BASED PROCESS SIMULATION FOR COPPER 10100

5.1 Finite Element Simulations using Deform-2D

Finite Element simulation software Deform-2D is utilized for physics-based simulation modeling for orthogonal cutting copper 10100. Two-dimensional mechanics of orthogonal cutting process using Deform-2D follows the configuration given in Figure 1.3 in which the cutting tool and workpiece positioned against each other. Gradual movement of workpiece towards cutting tool models cutting motion during thermal-mechanical workpiece deformations. Assuming plane strain deformation, vertical location of the cutting tool in 2D simulation signifies the feed or undeformed chip thickness. The deformation behavior of the elements and their interactions during the simulation of the cutting process, ascertains the field output parameters through elastic-plastic deformation behavior of the work material such as displacement, strain, strain rate, stress, and force, and through the thermal solution the temperature. Having satisfactory progress in simulation and appropriate quantities of reliable outputs, the Finite Element modeling results is compared to experimental results for validation purposes. The two-dimensional Finite Element simulations were developed using updated Lagrangian method in which chip separation from workpiece is achieved with continuous remeshing. Deform-2D software is capable of handling global remeshing where needed through displacement boundary conditions defined for the workpiece. Therefore, in the model with Deform-2D, the left side of the workpiece boundary nodes is fixed in x-direction, and the bottom size of the workpiece boundary nodes is fixed in y-direction.

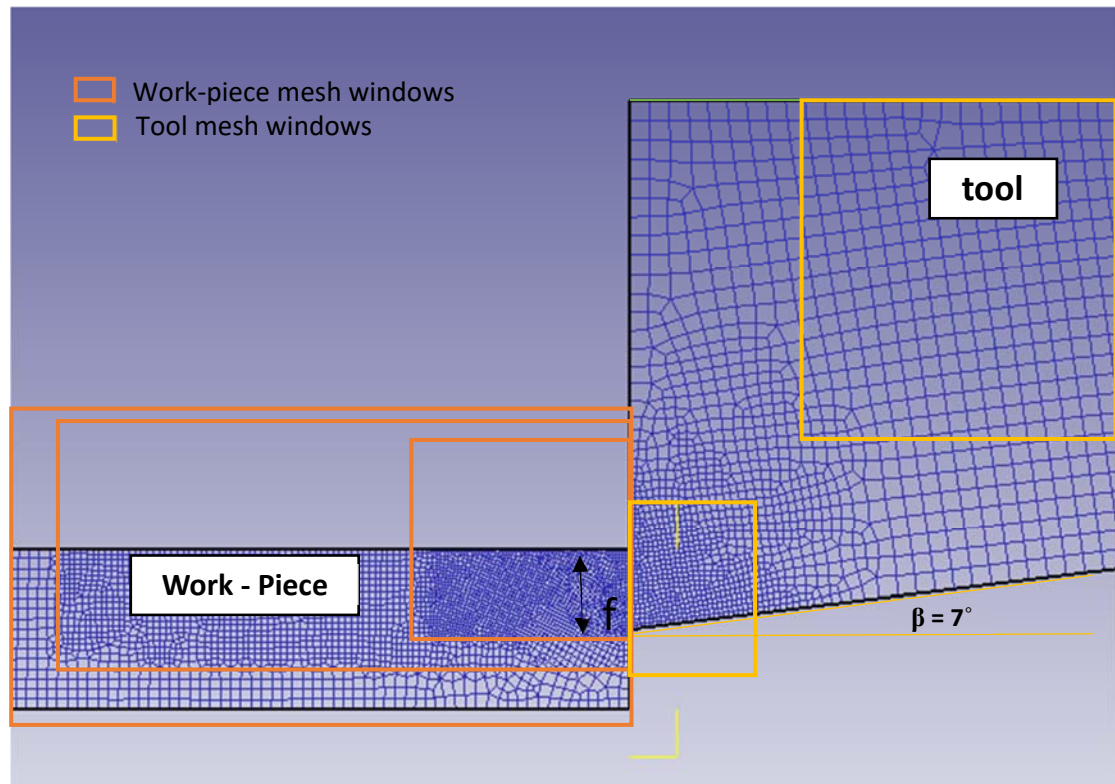


Figure 5.1 Workpiece and tool mesh using Deform-2D.

In the simulation with Deform-2D, the tool is moved to penetrate through the workpiece to create first deformation and a chip formation through the rake face of the cutting tool. However, the formation of chip is somewhat different in Deform-2D simulations. While the tool penetrates the workpiece, the workpiece elements around the tip of the cutting tool that are severely distorted are replaced via remeshing whenever they reach a critical strain value.

5.2 Designing Serrated Chip Formation Simulation using Deform-2D

In this case, a synthetic diamond cutting tool with nearly sharp cutting edge (tool edge radius $r_\beta = 0.0001$ mm) was utilized. The properties for synthetic diamond material were taken from the Deform software database for the tool “Diamond” (see Table 5.1). While thermal properties of copper 10100 were taken from the Deform software database and left unchanged, elastic and plastic properties were modified according to the quasi-static tensile test data obtained and material constitutive model parameters identified respectively. There was no coating layer

assigned on the cutting tool. Tool geometry such as a rake angle of $\gamma_1 = 0^\circ$ and a clearance angle of $\alpha = 7^\circ$ were assigned as per experimental cutting conditions considered. Workpiece dimensions included a range of workpiece width between 0.8 mm and 1 mm and workpiece height between 0.08 mm and 0.10 mm. These were implemented in FE simulation model depending upon the feed value in that cutting condition.

Table 5.1 Thermal and mechanical properties (at room temperature 20°).

Material Properties	Copper 10100	Single crystal diamond
Young's modulus [MPa]	91937	9e5
Poisson's ratio	0.396	0.2
Thermal expansion [$\text{mm} \cdot \text{mm}^{-1} \cdot ^\circ\text{C}^{-1}$]	1.70e-05	1.18E-06
Conductivity ($\text{W} \cdot \text{m}^{-1} \cdot ^\circ\text{C}^{-1}$)	390.987	2000
Density (kg/mm^3)	8.89E-09	3.52E-09
Specific heat ($\text{N} \cdot \text{mm} \cdot \text{kg}^{-1} \cdot ^\circ\text{C}^{-1}$)	0.385e6	0.508e6

Mesh definition and design is one of the essential parameters affecting output field variables in finite element simulations. Total of 4000-5000 elements were used to mesh workpiece and various mesh windows were used to define dense mesh along the tool-workpiece contact as shown in Fig. 5.1. The relative tool mesh size was defined between element size of 0.00833 and 0.04 while relative workpiece mesh size was defined between 0.004 and 0.012, starting from tool-workpiece contact area to the outer surface respectively. Cutting conditions defined in Table 3.3 were assigned to generate each simulation.

5.3 Constitutive Material Model for Copper 10100

In thermal-mechanical processing of workpiece material during machining process, localized flow softening phenomenon can occur which can be described as offering less resistance to local plastic deformations due to rearrangement of dislocations caused by subsequent cycling or dynamic recrystallization in the material. This phenomenon is usually observed during an increase in strain beyond a critical strain value together with a rapid rise in material's temperature. Flow softening is believed to cause adiabatic shearing within the primary shear zone. Thus, chip

segmentation with shear bands are formed as the deformed material leaves this zone (Calamaz et al., 2008; Sima & Özel 2010).

For this reason, modified material constitutive models with flow softening resulting from strain softening and temperature softening have influence on chip formation shape. In previous studies, several researchers (Calamaz et al., 2008; Sima & Özel 2010), were able to develop such a constitutive model and implemented it in FE simulation software (Forge-2D and Deform-2D respectively) to simulate serrated chip formation during cutting of titanium alloy Ti6Al4V.

5.3.1 Identification of JC material model parameters for copper 10100

A combined methodology defined in (Johnson & Cook 1983; Özel & Ulutan 2013; Wang et al., 2015,) was used to identify JC material model parameters for copper 10100. On this methodology, the flow stress data obtained from quasi-static tensile tests and combined from flow stress data calculated in orthogonal cutting tests. Shear strain, shear strain rate and shear stress identified from orthogonal cutting tests (Table 3.7), was utilized to calculate true strain, true strain rate and true shear stress. The stress-strain data was taken from separately performed quasi-static tensile tests at various tensile test apparatus crosshead speeds (0.2 in/min, 2 in/min, 5 in/min) and at different temperature 72 °F, 135 °F, 200 °F.

Both true stress-strain data from tensile tests and cutting experiments were used in a Matlab script defining and solving unknown Johnson-Cook material model parameters using least square method (Appendix A) to identify JC material parameters for copper 10100.

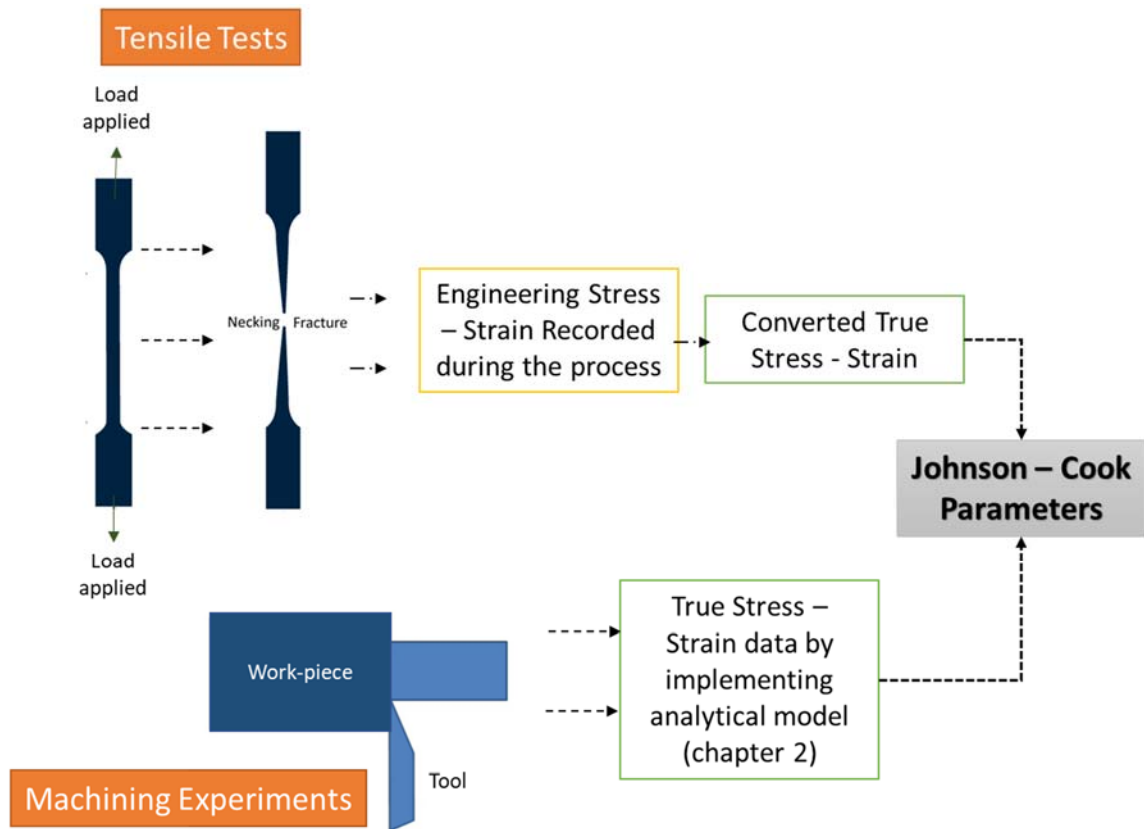


Figure 5.2 Graphical representation defining the methodology to obtain JC parameters.

Therefore, the Johnson-Cook material model parameters given in Table 5.2 were obtained using this methodology and adopted for the copper 10100 simulations. The flow stress curves at room temperature and at various strain rates using this Johnson-Cook material model are shown in Fig. 5.3.

Table 5.2 The Johnson-Cook material model parameters for copper 10100.

Johnson-Cook material model parameters		
A	543	[MPa]
B	1146.81	[MPa]
C	0.04498	[-]
n	0.52052	[-]
m	0.04056	[-]

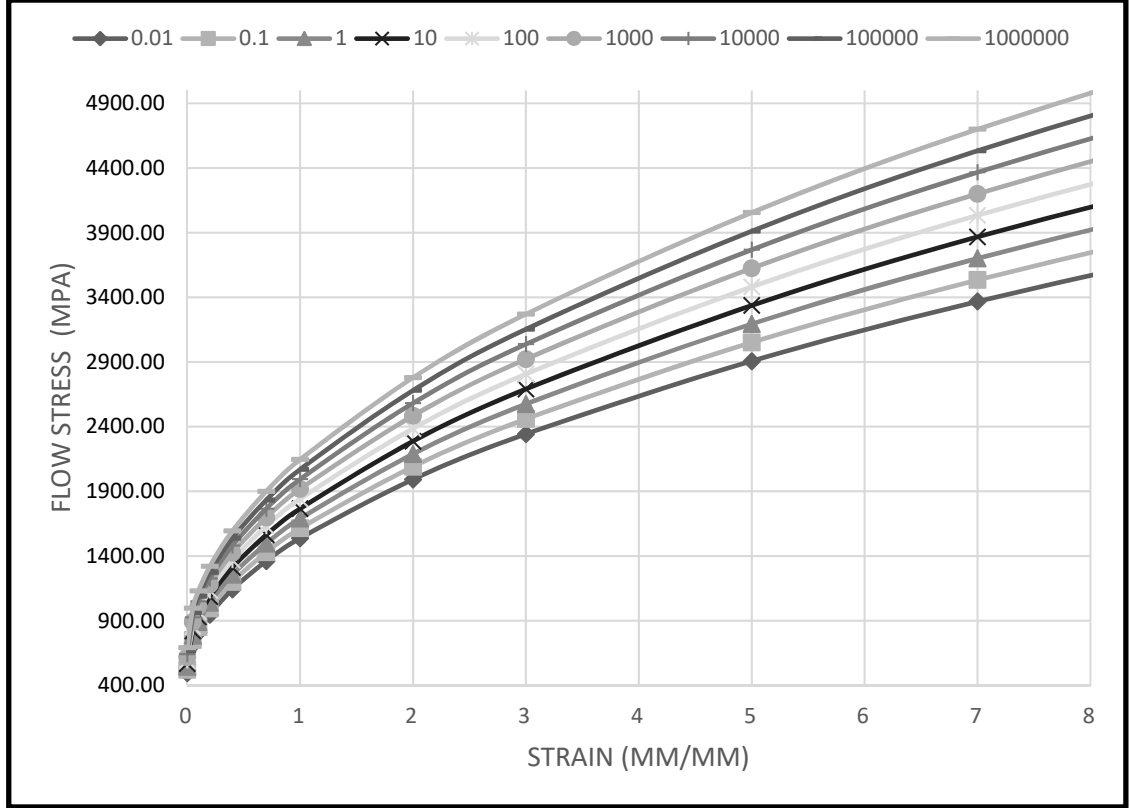


Figure 5.3 Flow stress curve for given JC parameters at room temperature (20 °C).

5.3.2 Modified material model with temperature dependent parameters and strain softening

Further modifications to the strain hardening part of the JC material model by including flow softening at higher strain values are proposed and the model is given in Eq. (5.1).

$$\bar{\sigma} = [A + B(\bar{\epsilon})^n][1 + C \ln(\frac{\bar{\epsilon}}{\bar{\epsilon}_0})] [1 - (\frac{T - T_0}{T_m - T_0})^m] [M + (1 - M)[\tanh(\frac{1}{(\bar{\epsilon} + P)^r})]^s] \quad (5.1)$$

This model is almost identical to the model modified by Calamaz et al. (2008) and the model modified by Sima & Özel (2010). Here an exponent “S” is introduced to further control hyperbolic tangential function for thermal softening.

Again, the JC model parameter values defined in Table 5.1 were taken as the base for this modified Johnson-Cook material model (Calamaz et al., 2008). In this modified model a multiplicative term is added to the strain hardening part, causes dependency of flow softening phenomenon not only upon temperature, but also on strain, as it can be seen in Fig. 5.4. This additional term affects the softening behavior of flow stress at a controlled range of strain.

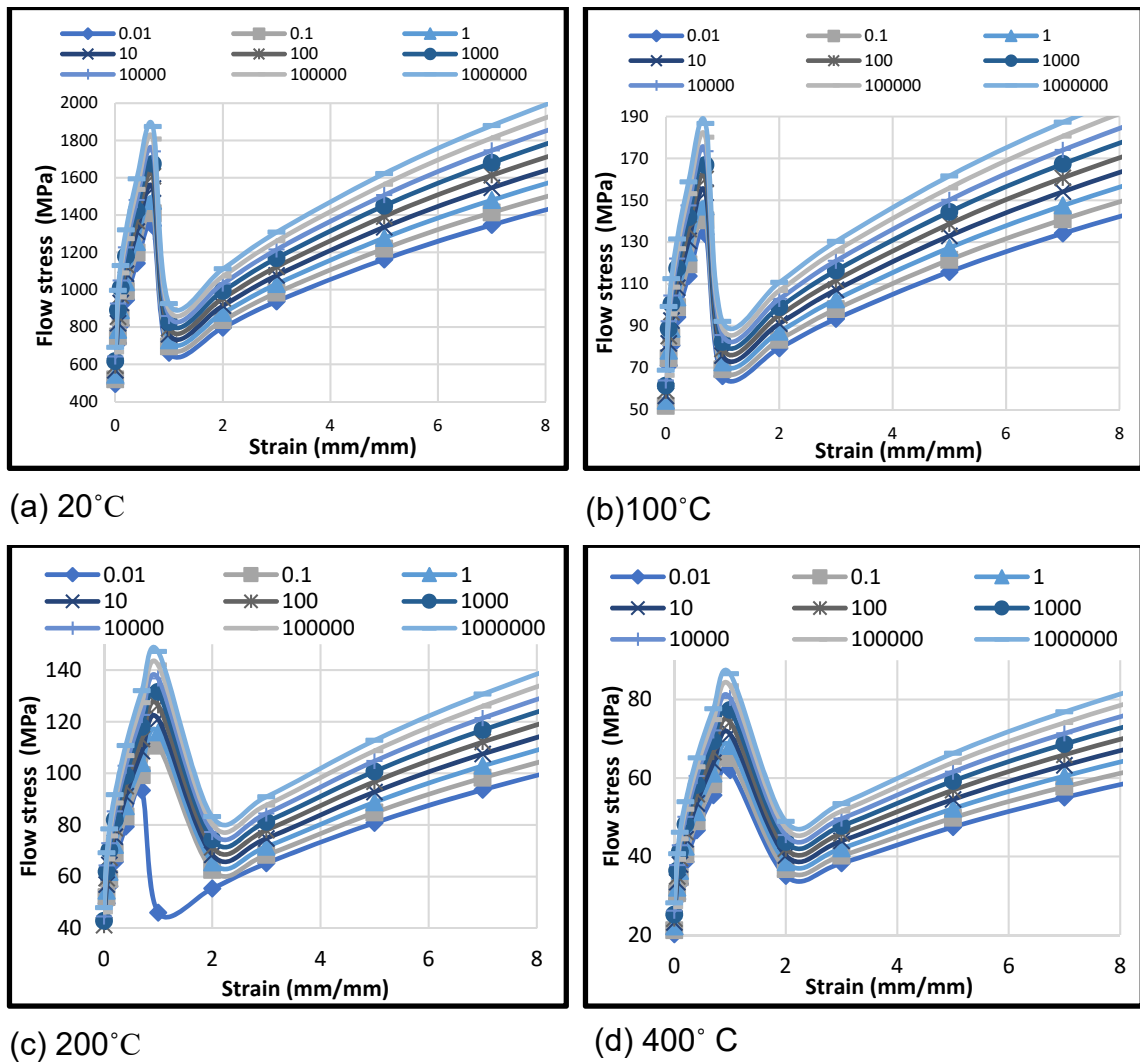


Figure 5.4 Thermal softening flow stress curves at temperature.

In order to identify the flow softening model parameters in this model, the effects of parameters M , S , p and r on the flow stress curves at high strain ranges and high temperatures were studied, while maintaining a good agreement between the model generated flow stress curves from analytical model values and quasi-static tensile tests values.

In order to study the effects of the parameters used in the flow softening terms (either the ones added to thermal softening part or strain hardening part), one parameter is varied while other parameters are held constant. After several trials with Deform-2D simulations, the following parameters were adopted.

Table 5.3 Thermal softening parameters determined for copper 10100.

M	0.4
S	5
p	0.1
r	5

The values derived from the flow stress curves (Fig 5.5) were altered with the existing flow stress values for copper 10100 in Deform-2D software database.

5.4 Consideration of Friction and Damage

A scientific approach of how one can define coefficient of friction in finite element (FE) simulations is defined in section 4.2.1. A gradient based friction method (Eq. 5.2) which takes experimental forces (cutting and thrust forces) in consideration was used to identify value of coulomb friction used in simulations.

$$\mu = \tan \left[\tan^{-1} \left(\frac{dF_t}{dF_c} \right) + \gamma_1 \right] \quad (5.2)$$

The average value of $\mu = 0.2$ was taken for all copper 10100 simulations.

In Deform-2D, different damage models can be defined and among those maximum principal stress to ultimate tensile stress criteria (Eq. 5.2) was used to initiate the replacement of distorted elements for separating the chip from the workpiece. A critical damage value, C_d , is used as 0.781 which was found from the data obtained from the tensile testing of copper 10100.

$$C_d = \frac{\sigma_{max}}{\sigma_{uts}} \quad (5.3)$$

5.5 Results and Discussions

All cutting conditions in the orthogonal cutting tests were simulated by using the Deform-2D FE model describe in the previous sections. Predicted forces from these FE simulations are compared with measured results as shown in Fig. 5.5.

Almost all cutting parameters (cutting speed and feed) have important effects on the cutting forces. The cutting forces slightly increased with the cutting speed and majorly increased with the feed. It was observed that measured thrust forces are increased sustainably at higher feed. From the comparison of simulated and measured cutting forces in Fig. 5.5, it is obvious that cutting and thrust forces are not in close agreements as simulated forces are half in values as of experimental forces.

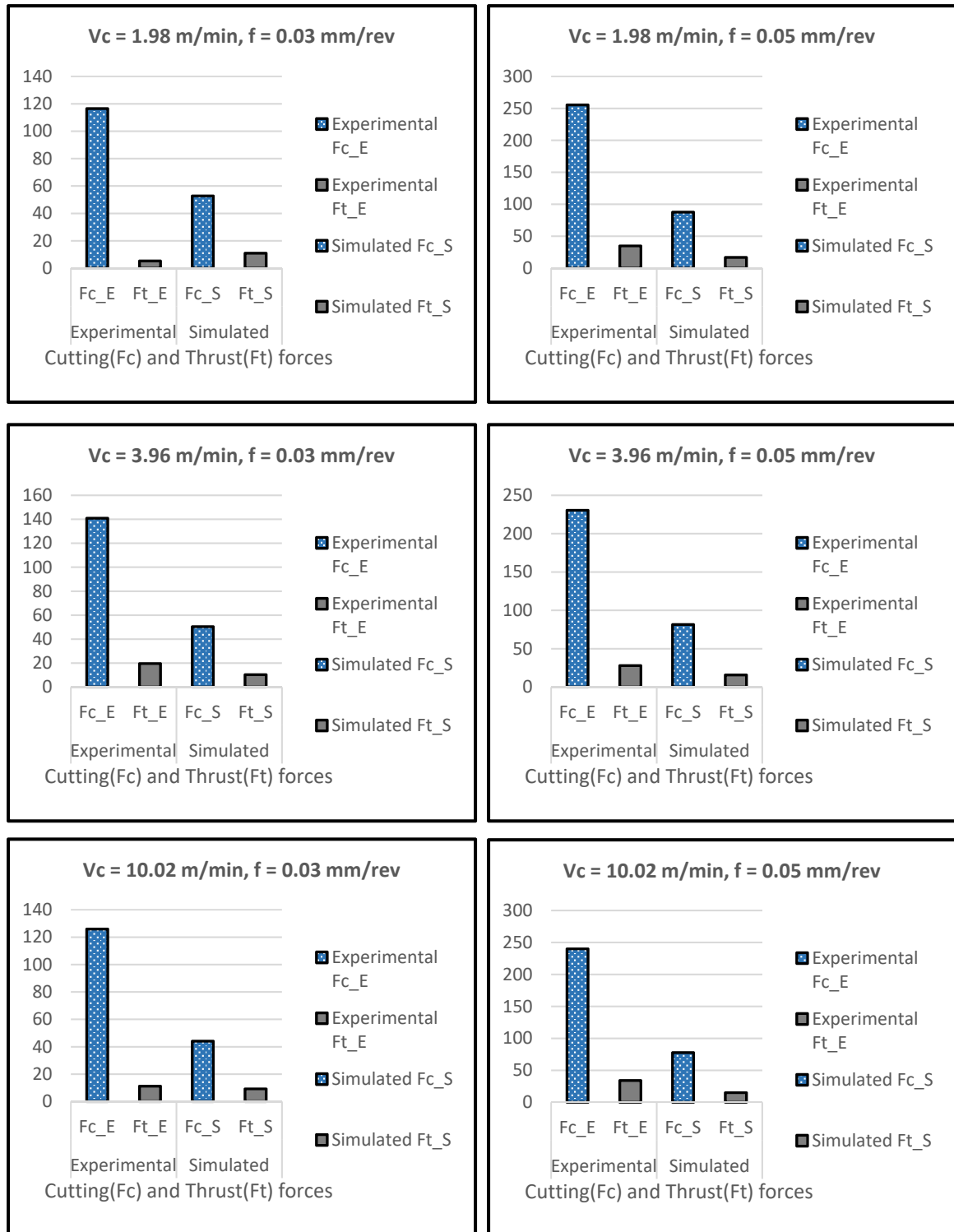
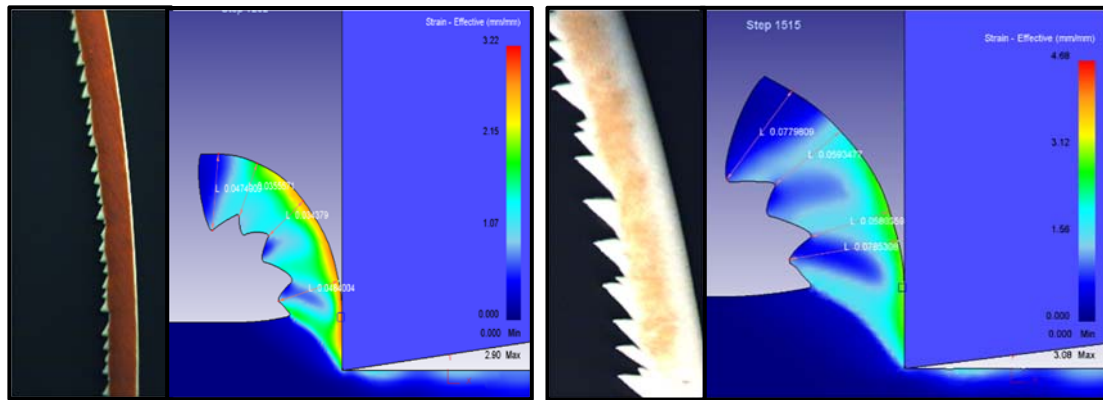


Figure 5.5 Comparison of experimental and simulated forces for copper 10100.

A detailed comparison of simulated serrated chips with microscopic chip images is shown in Fig. 5.6 for four of these cutting conditions. The results of measured and simulated serrated chip are given in Table 5.4. It is observed that almost all simulated chip geometries investigated depict periodic formation of serrated and uniform sized chip segments after a large single segment. A further investigation could be done to develop a simulation model with less error of margin with the experimental model.

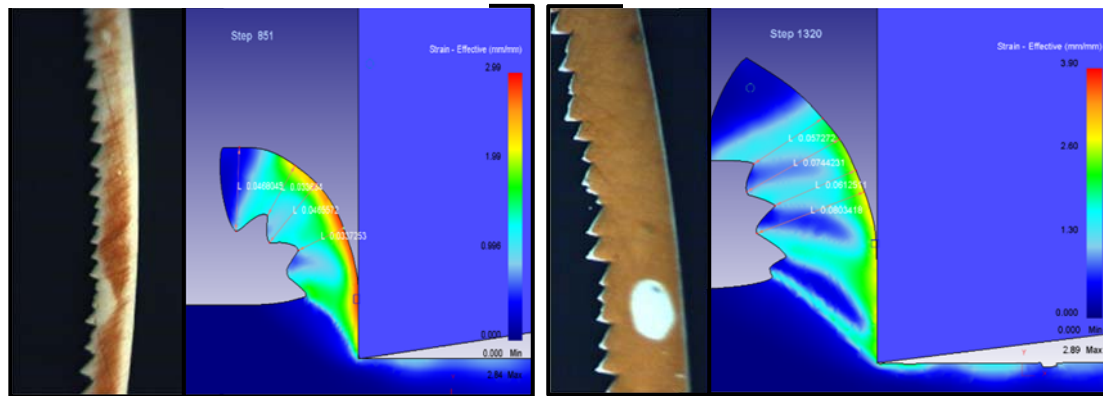
Table 5.4 The results of measured and simulated thickness values for serrated chips of copper 10100.

Tool material	Rake angle, γ_1 [degree]	Cutting speed, v_c [m/min]	Feed, f [mm/rev]	Experimental chip thickness		Simulated chip thickness	
				t_{min} [mm]	t_{max} [mm]	t_{min} [mm]	t_{max} [mm]
Diamond	0	3.96	0.03	0.026	0.033	0.034	0.047
Diamond	0	3.96	0.05	0.044	0.057	0.058	0.077
Diamond	0	10.02	0.03	0.028	0.033	0.033	0.046
Diamond	0	10.02	0.05	0.036	0.058	0.057	0.074



(a) Diamond Insert,
 $v_c = 3.96$ m/min
 $t = 0.03$ mm

(b) Diamond Insert,
 $v_c = 3.96$ m/min
 $t = 0.05$ mm



(c) Diamond Insert,
 $v_c = 10.02$ m/min
 $t = 0.03$ mm

(d) Diamond Insert,
 $v_c = 10.02$ m/min
 $t = 0.05$ mm

Figure 5.6 Comparative study of experimental and simulated chips for copper 10100.

CHAPTER 6

CONCLUSION AND CONTRIBUTIONS

Finite Element simulations of orthogonal metal cutting operations have been performed and verified with experiments during this work. The following can be concluded according to the observations made during the thesis, which may be seen as a summary.

In this research work, a material ductile failure based finite element simulation modeling for high speed cutting of titanium alloy Ti6Al4V and a modified constitutive material model-based FE simulation for copper 10100 are proposed. Material separation to form chips and chip serration are modelled by utilizing both ductile failure and damage models for titanium alloy Ti6Al4V simulations while thermal softening parameters were utilized to model chip serration for copper 10100 simulations. The effect of cutting parameters such as cutting speed, feed, coating condition on cutting forces was studied. Following specific conclusions can be made from the study.

- The cutting parameters (cutting speed and feed) and tool coating (uncoated and TiAlN coated) have important effects on the cutting forces. The cutting forces generally increased with feed for both the materials. The experimental forces were verified with the FE simulations.
- Physics based process simulation model was developed for both the materials, titanium alloy Ti6Al4V and copper 10100. Constitutive material model, ductile failure model parameters and friction coefficient were identified for both copper 10100 and titanium alloy Ti6Al4V using finite element simulations.
- The cutting and thrust forces were found to be higher when cutting with coated tools in titanium alloy Ti6Al4V experiments which can be explained with a larger edge roundness created by the coating layer.
- Simulation results are more likely to match with the high cutting speed experiment (titanium alloy Ti6Al4V) results. There are some disagreements between experimental and simulated forces for copper 10100. The important parameters affecting the simulated forces are flow stress curve and the

coefficient of friction. A further investigation to identify an unprecedented flow stress curve for copper 10100 can be done to gain more similarity between experimental and simulated results.

REFERENCES

- Arrazola, P.J., Garay, A., Iriarte, L.M., et al. (2009) Machinability of titanium alloys (Ti6Al4V and Ti555. 3), *Journal of Materials Processing Technology* 209 (5): 2223-2230.
- Arrazola, P.J., Özel, T., Umbrello, D., Davies, M., Jawahir, I.S. (2013) Recent Advances in Modelling of Metal Machining Processes, *CIRP Annals-Manufacturing Technology*, 62 (2), 695–718.
- Atkins, A.G. (2005) Toughness and Cutting: a new way of simultaneously determining ductile fracture toughness and strength, *Engineering Fracture Mechanical* 72: 849–860.
- Boothroyd, G. (1981) *Fundamentals of Machining and Machine Tools*, Washington: Scripta Book Company.
- Calamaz, M., Coupard, D., Girot, F. (2008) A new material model for 2D numerical simulation of serrated chip formation when machining titanium alloy Ti–6Al–4V, *International Journal of Machine Tools and Manufacture*, 48(3-4): 275-288.
- Chen, G., Ren, C., Yang, X., et al. (2011) Finite element simulation of high-speed machining of titanium alloy (Ti-6Al-4V) based on ductile failure model, *The International Journal of Advanced Manufacturing Technology*, 56(9-12): 1027-1038.
- Childs, T., Maekawa, K., Obikawa, T., Yamane, Y. (2000) *Metal machining: theory and applications*, John Wiley & Sons Inc.
- Childs, T.H.C., Arrazola, P.J., Aristimuno, P., et al. (2018) Ti6Al4V metal cutting chip formation experiments and modelling over a wide range of cutting speeds, *Journal of Materials Processing Technology*, 255: 898-913.
- Cockcroft, M.G., Latham D.J. (1968) Ductility and the Workability of Metals, *Journal of Institute of Metals*, 96: 33–38.
- Cotterell, M., Byrne, G. (2008) Dynamics of chip formation during orthogonal cutting of titanium alloy Ti–6Al–4V. *CIRP Annals Manufacturing Technology*; 57(1): 93–96.

- Ernst, H., Merchant, M.E. (1941) Chip Formation, Friction and High-Quality Machined Surfaces Transactions of American Society for Metals, 29: 299–378.
- Fang, N., Yang, J., Liu, N. (2004) Analytical predictive modeling of serrated chip formation in high speed machining of 7075-T6 aluminum alloy. In: Proceedings of ASME International Mechanical Engineering Congress and Exposition, Anaheim, CA, 13–19.
- Grazka, M., Janiszewski, J. (2012) Identification of Johnson-Cook Equation Constants using Finite Element Method. Engineering Transactions, 60:215-223.
- Johnson, G.R., Cook, W. H. (1983) A constitutive model for metals subjected to large strains, high strain rates and high temperatures, In: Proceedings of the Seventh International Symposium on Ballistics, Hague, Netherlands, 54.
- Johnson, G.R., Cook, W.H. (1985) Fracture characteristics of three metals subjected to various strains, strain rates, temperatures and pressures Engineering Fracture Mechanics, 21: 31-48.
- Johnson, G.R., Holmquist, T.J. (1989) Test data and computational strength and fracture model constants for 23 materials subjected to large strains, high strain rates, and high temperatures. Los Alamos National Laboratory, Los Alamos, NM, Report No. LA-11463-MS.
- Karpat, Y., Özel, T. (2006) Predictive Analytical and Thermal Modeling of Orthogonal Cutting Process, Part I: Predictions of Tool Forces, Stresses and Temperature Distributions, ASME Journal of Manufacturing Science and Engineering, 128: 435-444.
- Kay, G. (2002) Failure modeling of titanium-6Al-4V and 2024-T3 aluminum with the Johnson-Cook material model, Technical Report, Lawrence Livermore National Laboratory, Livermore, CA.
- Klamecki, B.E. (1973) Incipient Chip Formation in Metal Cutting - A Three Dimension Finite Element Analysis, Ph.D. Thesis, University of Illinois at Urbana-Champaign, Urbana, IL.

- Lee, W.S., Lin, C.F. (1998) High-temperature deformation behavior of Ti6Al4V alloy evaluated by high strain-rate compression tests. *Journal of Materials Processing Technology*, 75(1-3): 127-136.
- Li, A., Pang, J., Zhao, J., et al. (2017) FEM-simulation of machining induced surface plastic deformation and microstructural texture evolution of Ti-6Al-4V alloy. *International Journal of Mechanical Sciences*, 123: 214-223.
- Melkote, S.N., Grzesik, W., Outeiro, J., Rech, J., Schulze, V., Attia, H., Arrazola, P.J., M'Saoubi, R., Saldana, C. (2017) Advances in material and friction data for modelling of metal machining, 66: 731 – 754.
- Meyer, Jr. H.W., Kleponis, D.S. (2001) Modeling the high strain rate behavior of titanium undergoing ballistic impact and penetration. *International Journal of Impact Engineering*, 26(1-10): 509-521.
- Obikawa, T., Usui, E. (1996) Computational machining of titanium alloy—finite element modeling and a few results. *Journal of Manufacturing Science and Engineering*, 118(2): 208-215.
- Oxley, P.L.B. (1989) *Mechanics of Machining*. Chichester: Ellis Horwood.
- Özel, T., Ulutan, D. (2013) Effects of machining parameters and tool geometry on serrated chip formation, specific forces and energies in orthogonal cutting of nickel-based super alloy Inconel 100, *Proceedings of the Institution of Mechanical Engineers Part B: J Engineering Manufacture*, 228: 673–686.
- Özel, T., Zeren, E. (2006) A Methodology to Determine Work Material Flow Stress and Tool-Chip Interfacial Friction Properties by Using Analysis of Machining. *ASME Journal of Manufacturing Science and Engineering*, 128: 119-129.
- Pawade, R.S., Joshi, S.S., Brahmkar, P.K. et al. (2007) An investigation of cutting forces and surface damage in high-speed turning of Inconel 718, *Journal of Materials Processing Technology*, 192–193: 159–146.
- Seo, S., Min, O., Yang, H. (2005) Constitutive equation for Ti–6Al–4V at high temperatures measured using the SHPB technique, *International journal of impact engineering*, 31(6): 735-754.
- Sima, M., Özel, T. (2010) Modified material constitutive models for serrated chip formation simulations and experimental validation in machining of titanium

- alloy Ti–6Al–4V, *International Journal of Machine Tools and Manufacture*, 50(11): 943-960.
- Subbiah, S., Melkote, S.N. (2007) Evaluation of Atkins' model of ductile machining including the material separation component, *Journal of Materials Processing Technology*; 182: 398–404.
- Tay, A.E., Stevenson, M.G., DeVahl, D.G. (1974) Using the Finite Element Method to determine temperature distributions in orthogonal machining, *Procedia Institute of Mechanical Engineers* 188(55): 627-638.
- Teng, X., Wierzbicki, T. (2006) Evaluation of six fracture models in high velocity perforation, *Engineering Fracture Mechanics*, 73:1653-1678.
- Wang, Q., Liu, Z., Wang, B., et al. (2016) Evolutions of grain size and micro-hardness during chip formation and machined surface generation for Ti-6Al-4V in high-speed machining, *The International Journal of Advanced Manufacturing Technology*. 82 (9-12):1725-1736.
- Wierzbicki, T., Bao, Y., Lee, Y.W., Bai, Y. (2005) Calibration and evaluation of seven fracture models, *International Journal of Mechanical Sciences* 45: 719-43.
- Zetterberg, M. (2014) A critical overview of machining simulations in ABAQUS, Degree Project, KTH Royal Institute of Technology, Sweden.

APPENDIX A

Least Square Method

Least squares method was used in estimating the unknown coefficients in the flow stress equation given defined in section 4.3

$$\bar{\sigma} = (A + B\varepsilon^n) \left(1 + C \ln \frac{\dot{\varepsilon}}{\dot{\varepsilon}_0} \right) \left[1 - \left(\frac{T - T_r}{T_m - T_r} \right)^m \right] \quad (\text{A.1})$$

$$\bar{\sigma} = \exp \left\{ \ln \left[(A + B\varepsilon^n) \left(1 + C \ln \frac{\dot{\varepsilon}}{\dot{\varepsilon}_0} \right) \left[1 - \left(\frac{T - T_r}{T_m - T_r} \right)^m \right] \right] \right\} \quad (\text{A.2})$$

Two important approximations that we are going to use in the equation development are,

$$a^x \approx 1 + x \ln(a)$$

$$\ln(1 + x) \approx x$$

We get,

$$1 - \left(\frac{T - T_r}{T_m - T_r} \right)^m = -m \ln \left(\frac{T - T_r}{T_m - T_r} \right)$$

and,

$$1 + C \ln \left(\frac{\dot{\varepsilon}}{\dot{\varepsilon}_0} \right) = \left(\frac{\dot{\varepsilon}}{\dot{\varepsilon}_0} \right)^C$$

and,

$$\ln(A + B\varepsilon^n) = \ln(A) + \frac{B}{A} + \frac{Bn}{A} \ln(\varepsilon)$$

While Johnson-Cook flow stress model is not linear, by a log transformation, the model becomes,

$$\ln(\bar{\sigma}) = \left[\ln(A) + \frac{B}{A} \right] + \left[\frac{Bn}{A} \right] \ln(\varepsilon) + C \ln \left(\frac{\dot{\varepsilon}}{\dot{\varepsilon}_0} \right) + (-m) \ln \left(\frac{T - T_r}{T_m - T_r} \right) \quad (\text{A.3})$$

where, $T=20^\circ\text{C}$ (room temperature) can be used from the room temperature, and $\dot{\varepsilon}_0 = 1 \text{ sec}^{-1}$ can be used for reference strain.

The linear model with the error associated results in,

$$\hat{Y} = \beta_0 + \beta_1 X_1 + \beta_2 X_2 + \beta_3 X_3 + \varepsilon \quad (\text{A.4})$$

Where, the coefficients are,

$$\beta_0 = \ln(A) + \frac{B}{A}$$

$$\beta_1 = \frac{Bn}{A}$$

$$\beta_2 = C$$

$$\beta_3 = -m$$

and independent variables are;

$$X_1 = \ln(\varepsilon)$$

$$X_2 = \ln\left(\frac{\dot{\varepsilon}}{\dot{\varepsilon}_0}\right)$$

$$X_3 = \ln\left(\frac{T - T_r}{T_m - T_r}\right)$$

The least squares method is aimed at finding estimates of $\beta_0, \beta_1, \beta_2, \beta_3$.

The solution can be written using a matrix notation where, Y is a matrix of measured flow stress values, X is the matrix of independent variables such as temperature, strain, strain rate

$$Y = \begin{bmatrix} Y_1 \\ Y_2 \\ \vdots \\ Y_n \end{bmatrix}, \text{ and } X = \begin{bmatrix} 1 & X_{11} & X_{21} & X_{31} \\ 1 & X_{12} & X_{22} & X_{32} \\ \vdots & \vdots & \vdots & \vdots \\ 1 & X_{1n} & X_{2n} & X_{3n} \end{bmatrix} \quad (\text{A.5})$$

The solution is found by differentiating the squared error with respect to the model parameters. Setting the resulting linear equations equal to zero leads to final solution,

$$\hat{\beta} = (X^T X)^{-1} (X^T Y) \quad (\text{A.6})$$

where, X^T is the transpose of the matrix X and $(X^T X)^{-1}$ is the inverse of the matrix $X^T X$.